KIT

Karlsruhe Institute of Technology

Characterization of the KATRIN Silicon Wafers with the Iron Bird test setup

Master's Thesis of

Sebastian Schmid

at the Department of Physics
Institute of Experimental Particle Physics (ETP)

Reviewer: Prof. Dr. Guido Drexlin
Second reviewer: Prof. Dr. Ulrich Husemann
Advisor: Dr. Florian Fränkle

01. June 2018 – 13. May 2019

Karlsruher Institut für Technologie
Fakultät für Physik
Wolfgang-Gaede-Str. 1
76131 Karlsruhe

I declare that I have developed and written the enclosed thesis completely by myself, and have not used sources or means without declaration in the text.
Karlsruhe, 13. May 2019

. . . .
(Sebastian Schmid)

Abstract

The KArlsruhe TRItium Neutrino experiment aims to determine the effective mass of the electron anti-neutrino by measuring the β-spectrum of molecular tritium. To reach the intended sensitivity of 0.2 eV/c^2 the energy spectrum close to the kinematic endpoint is determined precisely. To do so the experiment combines a high-luminosity windowless gaseous tritium source followed by a differential and cryogenic pump section for reduction of the tritium flow with a high resolution MAC-E filter spectrometer system. At the downstream end of the setup the transmitted electrons are detected by a focal plane detector system.

An important component of the KATRIN experiment is a segmented silicon wafer which counts the transmitted β-electrons. The wafer is installed at the end of a post acceleration electrode inside the KATRIN detector system. In the last years several detector wafers have been mounted to the Focal Plane Detector system. However, their performance was not entirely satisfactory. In order to examine the performance of silicon wafers before mounting it in the KATRIN Focal Plane Detector system a test stand, called Iron Bird, was established at KIT. Of particular importance is the determination of the energy resolution of individual pixels. For this purpose the Iron Bird utilizes readout electronics and a data acquisition system equivalent to the KATRIN Focal Plane Detector system. Additionally a check for short circuits between adjacent pixels is necessary.

In this thesis the new established Iron Bird test setup was used in combination with a wafer testing device in order to characterize a new batch of two wafers, which arrived at KIT in 2019. In a first investigation both wafers were successfully tested on short-circuits between adjacent pixels with a wafer testing device. In order to investigate the energy resolution of the wafers they were installed in the Iron Bird test setup and examined using a ^{241}Am-source. Since a replacement of the currently installed wafer in the KATRIN FPD system is considered the new batch of wafers is checked for suitability.

Zusammenfassung

Beim **KA**rlsruhe **TRI**tium **N**eutrino Experiment versucht man durch gezielte Vermessung des Tritium-β-Spektrums die effektive Masse des Elektron-Antineutrinos zu bestimmen. Hierfür wird die Kinematik von Elektronen nahe des Endpunktes beim Zerfall von molekularem Tritium vermessen. Um die angestrebte Sensitivität von $0.2\,\mathrm{eV}/c^2$ zu erreichen, werden die Elektronen von einer gasförmigen fensterlosen Tritiumquelle über verschiedene Teilabschnitte durch einen Spektrometertank geleiten, in welchem diese energetisch gefiltert werden. Nur Elektronen mit ausreichender kinetischer Energie können das angelegte elektrische Potential überwinden und schlussendlich vom Fokalebenendetektor nachgewiesen werden.

Jedes Teilsystem des Experiments muss, um die gewünschte Sensitivität zu erreichen, mit ausreichender Performanz arbeiten. Beim Fokalebenendetektor detektiert eine Si-PIN-Diode jene β-Elektronen, die beim Zerfall von Tritium entstehen und das elektrische Potential überwinden konnten. In den letzten Jahren wurden verschiedene Detektorwafer im Fokalebenendetektorsystem benutzt, bis sich herausstellte, dass diese jeweils nicht vollständig den Anforderungen genügten. Um Wafer, bevor sie in das KATRIN Detektorsystem eingesetzt werden, auf ihre Performance hin zu überprüfen, wurde am KIT ein Teststand, genannt Iron Bird, entwickelt. Eine wichtige Kenngröße des Detektors ist die Energieauflösung seiner einzelnen Pixel. Hierfür verfügt der Iron Bird über die gleiche Auslese- und Datenerfassungssysteme wie das KATRIN Detektorsystem. Ebenfalls muss der Wafer auf Kurzschlüsse zwischen benachbarten Pixeln überprüft werden.

In dieser Arbeit wurde der neu entwickelte Iron Bird Teststand zusammen mit einem Wafer Testgerät benutzt, um eine 2019 gelieferte Charge an Wafern zu charakterisieren. Hierfür wurden die beiden gelieferten Wafer mit dem Wafer Teststand erfolgreich auf Kurzschlüsse zwischen Pixel überprüft. Zusätzlich wurden die Wafer mit einer im Iron Bird Teststand eingebauten ^{241}Am-Gammaquelle auf ihre Energieauflösung untersucht. Da im Moment ein Austausch des Wafers, welcher im KATRIN Detektorsystem eingebaut ist, erwägt wird, wurden die neuen Wafer auf ihre Eignung diesbezüglich getestet.

Contents

1 Neutrino Physics

Since the neutrino was postulated in 1930 a great development has happened in neutrino physics. Lots of physicists furthered and are furthering the research of this tiny particle in a great variety of experiments in order to study its properties and behaviour. It started with its postulation by W. Pauli [1] in 1930, was followed by its discovery in the Poltergeist experiment 27 years later [2], the phenomenon of neutrino oscillation in the late 1990s and the ongoing approaches to measure the neutrino mass. This Chapter guides through the history of neutrino physics during the last 90 years.

1.1 History of Neutrino Physics

In the beginning of the 20th century three types of radioactivity were known: α, β and γ-radiation. For α-radiation a discrete energy for the emitted particle was observed, depending on the decaying element. This monoenergetic spectrum was expected at β-radiation too. In 1914 J. Chadwick observed a continous energy spectrum in the β-decay of radium by using a detector, later known as Geiger-Mueller counter. The resulting spectrum is shown in Figure 1.1. Assuming a two body decay a continous spectrum would imply a violation of energy and momentum conservation. One solution of this problem is the introduction of a new particle. This has been done by W. Pauli, when he wrote an open letter to L. Meisner and the "Radioactive Ladies and Gentlemen" at a meeting in Tubingen [1]. This new particle, called "neutron", would be electrically neutral, spin-$\frac{1}{2}$ and be emitted together with the electron at the β-decay:

$$^{A}_{Z}X \rightarrow \, ^{A}_{Z+1}Y + e^{-} + \bar{\nu}_e \tag{1.1}$$
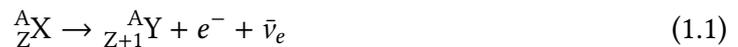
In 1932 J. Chadwick discovered the neutron as a part of the atomic nucleus by investigating an unknown radiation, emitted by beryllium after interacting with α-particles. With this background E. Fermi developed a theory for the three body decay as a point-like weak interaction in 1934:

$$n \rightarrow p + e^{-} + \bar{\nu}_e \tag{1.2}$$

He called the third particle $\bar{\nu}_e$ "neutrino", meaning the little neutral one [4].

In 1952 C. Cowan and F. Reines had the idea to use nuclear fission reactors as a strong source of neutrinos, since in one single fission an average of 6 neutrinos in the MeV-range is emitted [5]. With that high flux of neutrinos they planned to observe the inverse β-decay inside a water tank:

$$\bar{\nu}_e + p \rightarrow e^{+} + n \tag{1.3}$$
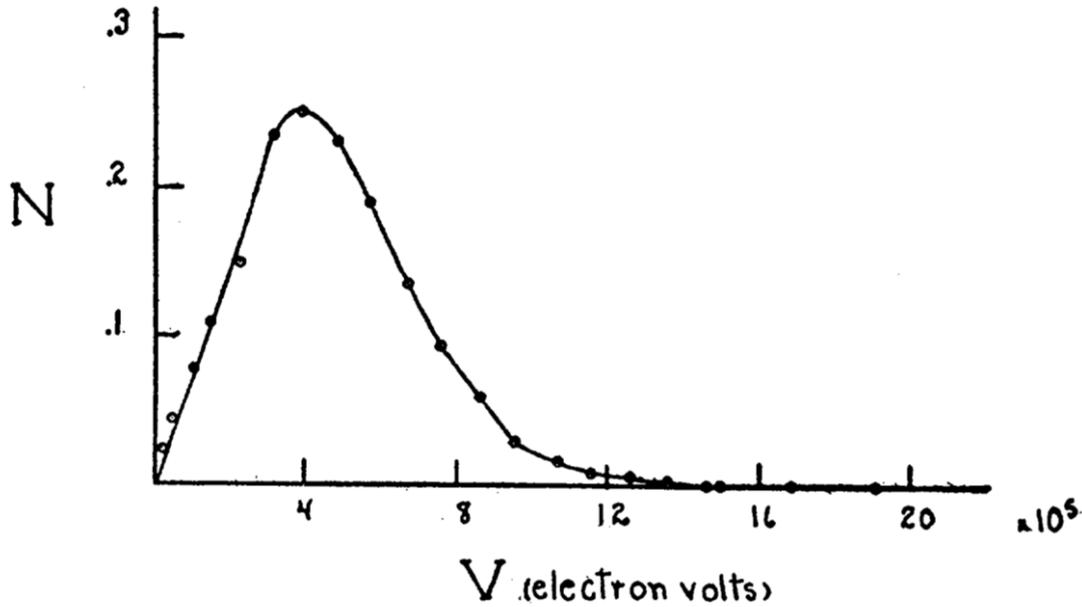
Figure 1.1: β-**spectrum of radium** measured by J. Chadwick in 1914. Figure adapted from: [3].

The generated positron annihilates with an electron by emitting two characteristic γ-photons with energies of 511 keV. They are detected via liquid scintillators and photomultipliers surrounding the water tank. The generated neutrons are moderated via scattering with the protons in the water and absorbed by cadmium. The excited cadmium nucleus emits a photon while its de-excitation to the ground state:

$$n + {}^{108}\text{Cd} \rightarrow {}^{109m}\text{Cd} \rightarrow {}^{109}\text{Cd} + \gamma \tag{1.4}$$
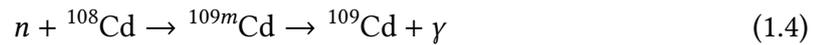
This delayed coincidence is used to discriminate the background from the neutrino events. A layer detector was used to detect the neutrino signals and veto background from cosmical muons. The cross section for inverse β-decay measured with this experiment was in good agreement with the theoretical expectations of $6.3 \times 10^{-44}\,\text{cm}^{-2}$ [2].

In 1962 a second type of neutrino was detected: the μ-neutrino. By bombarding a beryllium target with protons, accelerated by the Alternating Gradient Synchrotron at the Brookhaven National Laboratory, pions are generated. In-flight the pions decay into muons and μ-neutrinos:

$$\pi^+ \rightarrow \mu^+ + \nu_\mu \text{ and } \pi^- \rightarrow \mu^- + \bar{\nu}_\mu \tag{1.5}$$
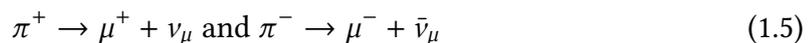
All particles except the neutrinos were shielded by 13.5m iron, whereas the neutrinos reached a 10-ton aluminum spark chamber detector. Due to the different shower shape, Schwartz, Lederman and Steinberger demonstrated, that only muon neutrinos were created in the detector, which proved the different nature of electron and muon neutrinos [6].
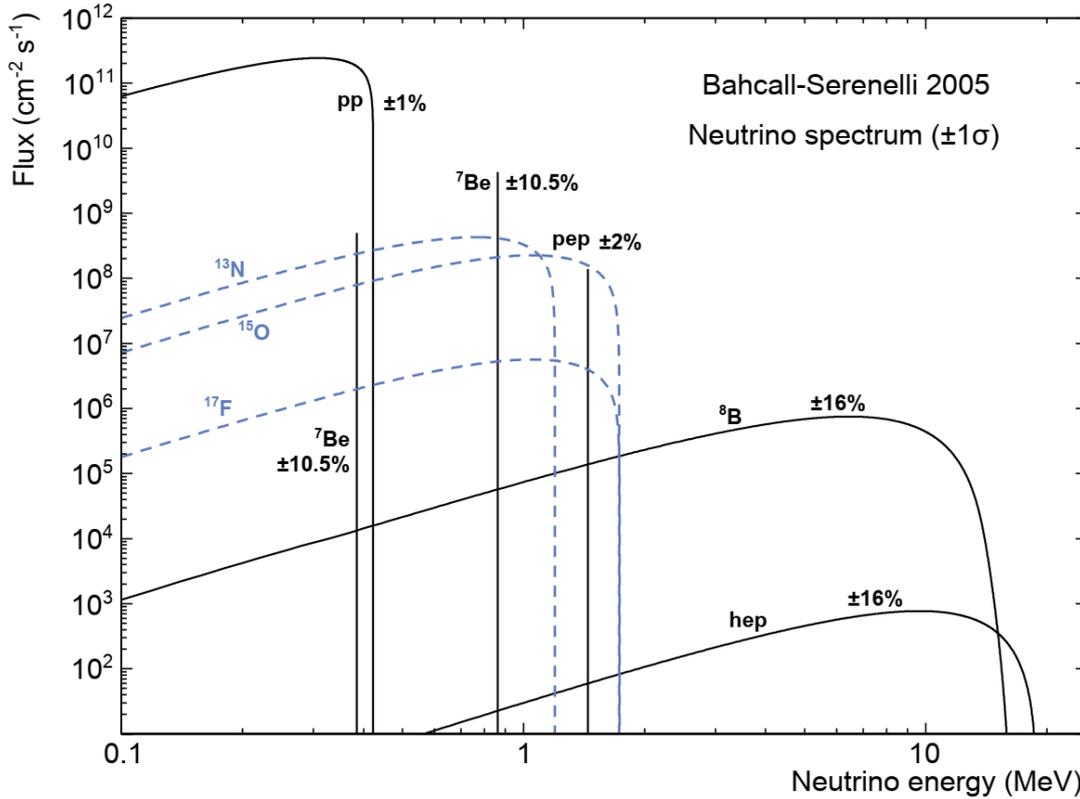
Figure 1.2: **Solar Neutrino flux** for different fusion processes, predicted by the standard solar model. Figure adapted from: [8].

By discovering the third lepton family in 1975 with the τ-lepton the necessity of a third neutrino was given. In 2001, 26 years later, the DONUT experiment could prove the existance of the τ-neutrinos at Fermilab. Therefor protons were accelerated to an energy of 800 GeV with the Tevatron collider and shooted on a tungsten beam dump. Particle showers containing unstable D_s mesons were created. The purely leptonic decay of D_s mesons and the subsequent decay of τ-leptons create τ-neutrinos:

$$D_S \rightarrow \tau + \bar{\nu}_\tau \tag{1.6}$$

After shielding the other particles the τ neutrinos were detected in emulsion plates via a characteristic kink in their trajectory within 2 mm of their point of creation. This indicates a high transverse momentum and gives a proof of their existance [7].

1.2 Phenomenon of Neutrino Oscillation

In the Standard Model of Particle Physics (SM) the three known neutrino generations (ν_e, ν_μ and ν_τ) are described as dublets with their leptonic partners (e^-, μ^- and τ^-) and transform under the weak isospin SU(2) gauge symmetry. In the 1960s attempts of unifying this symmetry group with the U(1) symmetry of the hypercharge Y were attempted.

Introducing masses into the SU(2) ⊗ U(1) group breaks the gauge invariance of the theory. By introducing a scalar Higgs-field which couples with the gauge fields of U(1) the mass is given by spontaneous symmetry breaking to the gauge bosons with mass ($W^{+/-}$, Z^0), while remaining the photon massless. This theory was finally proven by the discovery of the predicted Higgs boson at the LHC in 2012 [9] [10].

In 1956 C. S. Wu proved maximal violation of parity conservation in the weak interaction. As a result only left-handed particles and right-handed antiparticles couple to the weak gauge bosons [11]. In an experiment in 1958 M. Goldhaber and others determined the helicity of the neutrinos, which is the projection of the spin on the momentum of a particle, to be $h_\nu = -1 \pm 0.3$ [12]. This result confirmed the experiment of Wu in 1956 and implies the existence of only left-handed neutrinos and right-handed antineutrino, both massless in the SM.
By measuring the width of the Z-resonance at the LEP collider at CERN in 1989 the ALEPH experiment found evidence of three light types of neutrinos in the weak interaction 12 years before the discovery of the ν_τ [13].

In 1970 an experiment was developed in the Homestake Mine in South Dakota. A tank filled with 615 tons of tetrachloroethylene (C_2Cl_4) was used as target for neutrinos originating from the sun. The detection of the neutrinos was accomplished by the inverse β-decay of ^{37}Cl [14]:

$$\nu_e + {}^{37}\text{Cl} \rightarrow {}^{37}\text{Ar} + e^- \tag{1.7}$$

After a few weeks of exposure, the Argon atoms were extracted with radio-chemical procedures and stored. The Auger electrons emitted at the decay back to ^{37}Cl via electron capture were counted with proportional counters. The newly developed Solar Standard Model (SSM) by J. Bahcall [15], made precice predictions regarding the expected neutrino flux. In all measurements the Homestake experiment counted a significally lower rate of electron neutrinos compared to the expected rate. The 'solar neutrino deficit' was born. Later experiments like GALLEX [16], SAGE [17] and GNO [18], all together radio-chemical experiments, confirmed the missing neutrino flux.

Later the water-based Cherenkov experiment Kamiokande [19] detected the rates of electron and muon neutrinos in real-time. Finally the Sudbury Neutrino Observatory (SNO) could distinguish between the flavors and count the different rate with its 1000t heavy water tank. This experiment could measure the flux for charged current reaction (CC), neutral current interaction (NC) and via elastic scattering (ES) [20]:

$$\nu_e + \text{d} \rightarrow \text{p} + \text{p} + e^- \text{ (CC)} \tag{1.8}$$

$$\nu_x + \text{d} \rightarrow \text{p} + \text{n} + \nu_x \text{ (NC)} \tag{1.9}$$

$$\nu_x + e^- \rightarrow \nu_x + e^- \text{ (ES)} \tag{1.10}$$
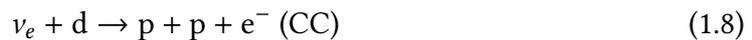
with x = e, μ, τ. The results showed the same deficit of electron neutrinos. In order to explain this deficit, neutrinos have to change their flavor while traveling from the

sun to earth. This phenomenon is called neutrino oscillation and was described by B. Pontecorvo in the 1960's. Like in the quark section, where the flavor eigenstates are not equal to the mass eigenstate of the particle, this concept was applied to neutrinos. Similar to the Cabbibo-Kobayashi-Maskawa (CKM) matrix in the quark sector describes the Pontecorvo–Maki–Nakagawa–Sakata (PMNS) matrix the mixing of the neutrino flavors. The eigenstates are then given by:

$$|v_\alpha\rangle = \sum_i U_{\alpha,\,i} |v_i\rangle \tag{1.11}$$

with $\alpha = e, \mu, \tau$, and i = 1, 2, 3. The parameterized PMNS matrix is given by:

$$\begin{pmatrix} 1 & 0 & 0 \\ 0 & c_{23} & s_{23} \\ 0 & -s_{23} & c_{23} \end{pmatrix} \begin{pmatrix} c_{13} & 0 & s_{13}e^{-i\delta} \\ 0 & 1 & 0 \\ -s_{13}e^{-i\delta} & 0 & c_{13} \end{pmatrix} \begin{pmatrix} c_{12} & s_{12} & 0 \\ -s_{12} & c_{12} & 0 \\ 0 & 0 & 1 \end{pmatrix} \tag{1.12}$$

with the three mixing angles $c_{ij} = \cos\theta_{ij}$, $s_{ij} = \sin\theta_{ij}$ and a CP violating phase δ. When a neutrino is created in an interaction, it is in a pure flavor eigenstate. The time evolution is then given by:

$$|v_i(t)\rangle = e^{-iE_i t} |v_i\rangle \tag{1.13}$$

and the flavor eigenstate at time t:

$$|v_\alpha(t)\rangle = \sum_i U_{\alpha,\,i} e^{-iE_i t} |v_i\rangle = \sum_{i,\beta} U_{\alpha,\,i} U^*_{\beta,\,i} e^{-iE_i t} |v_\beta\rangle \tag{1.14}$$

The probability for a neutrino with flavor v_α to change into another flavor v_β is then given by:

$$\mathrm{P}_{v_\alpha \to v_\beta}(t) = |\langle v_\beta(t)|v_\alpha(t)\rangle|^2 = \sum_{i,j} U_{\alpha,i} U^*_{\beta,i} U^*_{\alpha,j} U_{\beta,j} e^{-i(E_i - E_j)t} \tag{1.15}$$

In the ultra-relativistic case ($p_i \gg m_i$ and $E \approx p_i$) this equation simplifies to:

$$\mathrm{P}_{v_\alpha \to v_\beta}\left(\frac{L}{E}\right) = \sum_{i,j} U_{\alpha,i} U^*_{\beta,i} U^*_{\alpha,j} U_{\beta,j} e^{-i\left(\frac{\Delta m_{ij}^2)L}{2E}\right)} \tag{1.16}$$

where L is distance between the source and the detector, E the energy of the neutrino, $\Delta m_{ij}^2 = m_i^2 - m_j^2$ the difference of squared masses. With this formula one can determine the probability of appearance of a neutrino with flavor β depending on the mass splitting, energy and distance from the source. Assuming only two flavors the matrix reduces to a 2 x 2 form with only one remaining mixing angle θ:

$$\begin{pmatrix} v_\alpha \\ v_\beta \end{pmatrix} = \begin{pmatrix} \cos\theta & \sin\theta \\ -\sin\theta & \cos\theta \end{pmatrix} \cdot \begin{pmatrix} v_1 \\ v_2 \end{pmatrix} \tag{1.17}$$

The Probability of an oscillation into another flavor is then given by:

$$\mathrm{P}_{v_\alpha \to v_\beta}\left(\frac{L}{E}\right) = \sin^2(2\theta_{12}) \sin^2\left(\frac{\Delta m_{12}^2}{4} \frac{L}{E}\right) \tag{1.18}$$
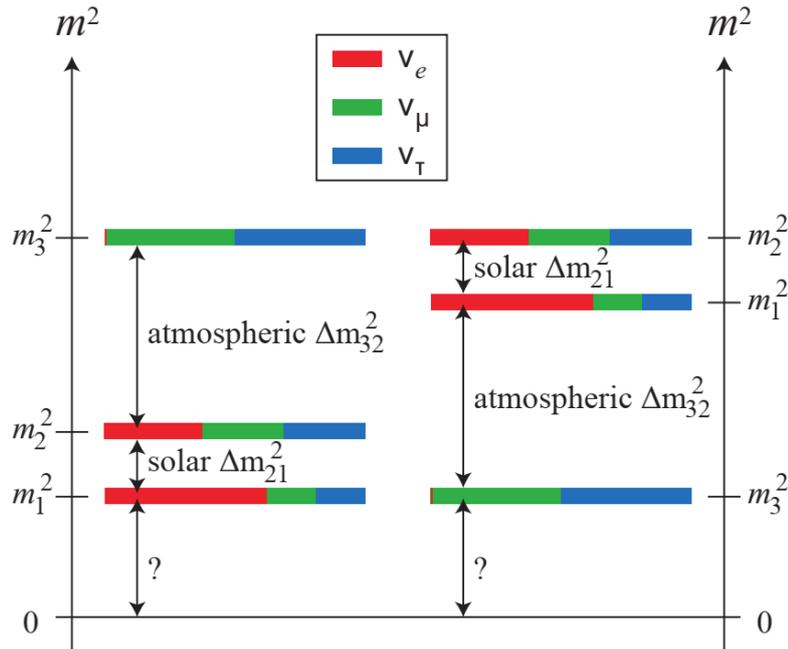
Figure 1.3: **left: The normal mass ordering with** $m_1 < m_2 \ll m_3$
right: The inverted mass ordering with $m_3 \ll m_1 < m_2$ Figure adapted
from: [22].

where θ_{12} is the mixing angle and $\Delta m_{12}^2 = m_1^2 - m_2^2$ is the mass splitting.

Additionally when traveling through matter the effective mass of the neutrino changes the oscillation property of the neutrino, due to coherent forward scattering with electrons. This effect is depending on the electrons density. In the sun this effect causes an additional transition between the neutrino eigenstates and is called Michejew-Smirnow-Wolfenstein (MSW) effect [21].

The discovery of neutrino oscillations had a great impact on neutrino physics, since neutrino oscillation implies neutrino masses of at least two of them, in contradiction to the standard model of particle physics.

There are generally two different types of experiments to investigate neutrino oscillation. Radiochemical experiments like Homestake [14], GALLEX [16] and GNO [18] make use of the inverse β-decay of chemicals and the later decay of excited nuclei. On the other hand are Cherenkov detectors, which can measure neutrinos via Cherenkov light, created by interaction of neutrinos transversing big water-filled tanks. In contrast to the radiochemical experiments it is possible to get real time and even spatial information of neutrinos with Cherenkov detectors.

In the upper atmosphere cosmic rays are producing a high multiplicity of particles with energies in the GeV range. Mainly protons interact with nuclei and produce pions and

kaons, which decay into muons:

$$\pi^+ \quad \to \mu^+ + \nu_\mu \to e^+ + \nu_\mu + \bar{\nu}_\mu + \nu_e \tag{1.19}$$

$$\pi^- \quad \to \mu^- + \bar{\nu}_\mu \to e^- + \bar{\nu}_\mu + \nu_\mu + \bar{\nu}_e \tag{1.20}$$

With this reactions approximately twice as many muon neutrinos than electron neutrinos are produces in the atmosphere. At the Super-Kamiokande experiment, the successor of the Kamiokande experiment, a huge tank filled with 50kt of water and with 11200 photomultiplier on its wall is used to detect neutrinos via Cherenkov light. With this setup it is possible to measure the direction of the incoming neutrinos, pointing to the source. With this principle the atmospheric neutrinos could be investigated angle dependent with the result of an up-down asymmetry in the rate of muon neutrinos [23]. This indicates a change of neutrino flavor while traveling through the earth.

Another source of neutrinos are nuclear fission reactors, which can provide a very high neutrino flux of up to 10^{21} s^{-1} in the range of a few MeV. In the decay chain in the reactor in average 6 electron anti neutrinos are generated per fission. By establishing one detector with a distance of 1 km and another with 2 km distance from the reactor it is possible to measure the mixing angle θ_{13} and the mass splitting Δm_{13}^2 in the disappearance channel of the electron anti neutrinos. Several experiments like Daya Bay in China [24] and Double Chooz [25] in France used this experiment design.

An important role in the neutrino physics is the mass ordering of the different neutrino masses. Since oscillation experiments can only measure differences of the squared masses, the sign of Δm_{23} could not be determined. In Figure 1.3 two different possibilities of the mass ordering are shown. Additionally a third, the quasi-degenerated ordering, is possible:

- normal mass ordering: $m_1 < m_2 \ll m_3$

- inverted mass ordering: $m_3 \ll m_1 < m_2$

- quasi-degenerated scenario: $m_1 \approx m_2 \approx m_3 \gg 10^{-3}$ eV^2

Combining the results of the previously shown experiments the following values for the mixing angles and mass splitting have been determined [26]:

$$\sin^2(\theta_{12}) \quad = \quad 0.310^{+0.013}_{-0.012} \tag{1.21}$$

$$\sin^2(\theta_{23}) \quad = \quad 0.580^{+0.017}_{-0.021} \tag{1.22}$$

$$\sin^2(\theta_{13}) \quad = \quad 0.02241^{+0.00065}_{-0.00065} \tag{1.23}$$

$$\Delta m_{21} \quad = \quad 7.39^{+0.21}_{-0.20} \cdot 10^{-5} \text{ eV}^2 \tag{1.24}$$

$$|\Delta m_{31}| \quad = \quad 2.525^{+0.033}_{-0.031} \cdot 10^{-3} \text{ eV}^2 \tag{1.25}$$
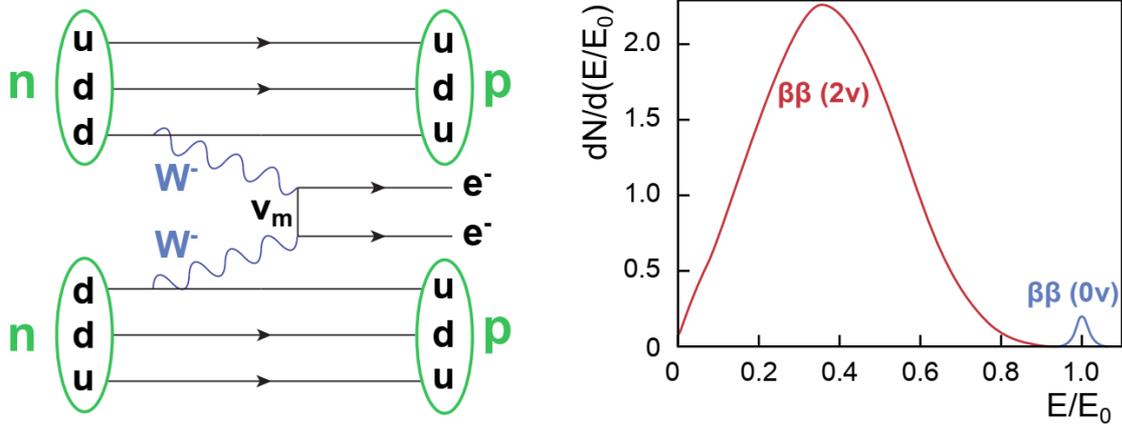
Figure 1.4: **left: Feynman graph for the neutrinoless double β-decay:** Two neutrons are transformed into protons by exchanging a virtual Majorana-like neutrino and emitting two electrons. Figure adapted from: [27].
right: Electron spectrum of the neutrino-afflicted and neutrinoless double β-decay: The spectrum of $0\nu\beta\beta$-decay is scaled with a factor of 0.2. The mono-energetic line is broadened to a peak due to detector effects. Figure adapted from: [28].

1.3 Measurement of the Neutrino Mass

The experiments shown in Section 1.1 and 1.2 can not provide a measurement on the absolute value of the neutrino masses. In order to do so there are different approaches in different physical domains.
One way is the investigation of the cosmic neutrino background (CνB) and the cosmic microwave background (CMB). The so called relic neutrinos originate from the time, when the weak interaction 'froze' out and the neutrinos decoupled from the primordial plasma. This happened, when the weak interaction rate dropped below the Hubble expansion rate at about 1 s after the Big Bang. The cosmic microwave background has its origin in the decoupling of photons from matter, when the universe expanded and cooled down below the energies, where photons could desintegrate deuterium atoms about 380 000 a after Big Bang at a temperature of 2.725 K. Due to their very low energies and consequently low interaction cross-section this relic neutrinos could not be detected yet. Using the estimations from the cosmological models one expect a relic neutrino density of 336 cm^{-1}. By comparing this value with the total energy density of the universe one can estimate the total mass of all neutrinos:

$$\sum_{i=1}^{3} m_i = 93\Omega_\nu \mathrm{h}^2 \mathrm{eV} \tag{1.26}$$

Measurements of the cosmic microwave background with the two satellites WMAP and Planck provide an upper limit of the sum of all neutrino masses, but are highly model-

dependent [29]:

$$\sum_{i=1}^{3} m_i \leq 0.23 \, \text{eV} \tag{1.27}$$

Double β-decay is a second-order process, where two protons or neutrons decay simultaneously in a nucleus:

$$^A_Z X \rightarrow \, ^A_{Z+2} Y + e^- + e^- + \bar{\nu}_e + \bar{\nu}_e \quad (2\nu\beta^-\beta^-) \tag{1.28}$$

$$^A_Z X \rightarrow \, ^A_{Z-2} Y + e^+ + e^+ + \nu_e + \nu_e \quad (2\nu\beta^+\beta^+) \tag{1.29}$$

This decay is possible, if the single β-decay is energetically forbidden. Assuming the neutrino to be a Majorana particle it is possible due to his non-existent electrical charge to be his own antiparticle. As a consequence two neutrinos, created in the double β-decay could absorb each other and the neutrinoless double β-decay would be possible. This implies a violation of lepton number conservation, which contradicts the SM. In Figure 1.4 the Feynman diagram of the $0\nu\beta\beta$-decay is shown, while on the right side the spectra of the neutrino-afflicted and the neutrinoless β-decay is shown. As a signature of the $0\nu\beta\beta$-decay the two electrons have a characteristic energy, since they carry away the surplus energy, respective the Q-value of the decay. One experiment using ^{76}Ge is GERDA, located in the Laboratori Nazionali del Gran Sasso (LNGS) with a Q-value of 2039 eV [30]. The appropriate reaction equation for the $0\nu\beta\beta$-decay is given by:

$$^{76}\text{Ge} \rightarrow \, ^{76}\text{Se} + e^- + e^- \tag{1.30}$$

In order to determine the neutrino rest mass with that kind of experiment, the measured quantity is the half life $T_{1/2}^{0\nu\beta\beta}$:

$$\left(T_{1/2}^{0\nu\beta\beta}\right)^{-1} = G^{0\nu\beta\beta}\left(Q, Z\right)) \cdot \left| M_{GT}^{0\nu\beta\beta} - \left(\frac{g_V}{g_A}\right)^2 M_F^{0\nu\beta\beta} \right|^2 \cdot \frac{\langle m_{\beta\beta}\rangle^2}{m_e^2} \tag{1.31}$$

where $G^{0\nu\beta\beta}$ corresponds to the phase-space integral, $M_{GT}^{0\nu\beta\beta}$ and $M_F^{0\nu\beta\beta}$ are the Gamov-Teller and nuclear matrix elements, g_V and g_A are the vector and axial-vector coupling constants of the electroweak interaction, m_e is the electrons mass and $\langle m_{\beta\beta}\rangle$ is the coherent sum of neutrino mass eigenstates:

$$\langle m_{\beta\beta}\rangle = \left| \sum_{i=1}^{3} U_{ei} m_i \right| \tag{1.32}$$

GERDA [30] and other experiments like MAJORANA [32] and CUORE [33] could not find any evidence of a neutrinoless double β-decay. The upper limit on the coherent sum of neutrino mass eigenstates in the GERDA experiment is given by [34]:

$$\langle m_{\beta\beta}\rangle < (0.12 - 0.26) \, \text{eV} \tag{1.33}$$

The single β-decay provides a method to measure the neutrino mass in a model-independent, well understood scenario. In this three-body decay an neutron converts into a proton by emitting an electron and a electron antineutrino:

$$^A_Z X \rightarrow \, ^A_{Z-1} Y + p + e^- + \bar{\nu}_e \tag{1.34}$$
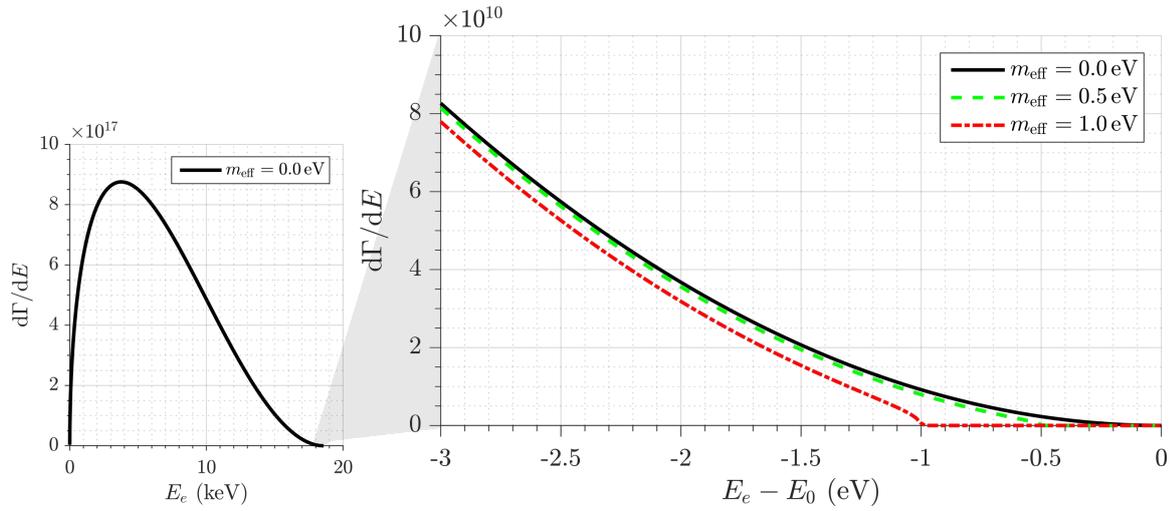
Figure 1.5: **left: β-spectrum of tritium** assuming a vanishing neutrino mass.
right: Endpoint of the tritium β-spectrum with different neutrino masses.
Figure adapted from: [31].

Due to energy conservation one can get access to the mass of the neutrino by measuring the energy spectrum of the β-electrons. In Figure 1.5 the β-spectrum of tritium is shown. On the right side the closeup of the endpoint is shown for different neutrino masses. The closer one approaches to the endpoint the bigger gets the discrepancy of the spectrum. At experiments in Troitsk and Mainz an upper limit on the mass of the electron antineutrino was set with this experimental method [35] [36]:

$$m_{\bar{\nu}_e} < 2\,\text{eV (95\% C.L.)} \tag{1.35}$$

By analyzing the endpoint of the β-spectrum of tritium with very high precision, the **KA**rlsruhe **TRI**tium **N**eutrino Experiment aims to determine the neutrino mass with an intended sensitivity of $0.2\,\text{eV}$ (95% C.L.).

2 The KATRIN Experiment

The KATRIN experiment is the next generation neutrino experiment, which aims to measure the neutrino mass by β-decay of tritium. By analyzing the shape of the β-spectrum close to the endpoint it is targeted to improve the sensitivity of previous experiments by one order of magnitude. To achieve a sensitivity of 0.2 eV (90% C.L.) the influence of a non-vanishing neutrino rest mass on the spectrum has to be resolved with high precision and low background. For this purpose KATRIN uses the principle of a MAC-E filter for the high-precise tritium energy spectroscopy. It combines an excellent energy resolution with a high angular acceptance for β-electrons, emitted by the decay of tritium. This Chapter gives an overview of the measurement principle of KATRIN in Section 2.1 and all of its subsystems in Section 2.2.

2.1 The MAC-E Filter Principle

To scan the endpoint at an energy of $E_0 = 18.6$ keV with high precision a combination of electric and magnetic fields is used. The **M**agnetic **A**diabatic **C**ollimation combined with an **E**lectrostatic (MAC-E) filter shown in Figure 2.1 guides the β-electrons with magnetic fields along the beamline, while the electricstatic filter applies a retarding potential for spectroscopy [37]. The adiabatic guidance from the source to the detector is provided by superconducting solenoid with high magnetic fields. To provide the electric fields, parallel to the magnetic field a negative high voltage is applied to the spectrometer. This forms a potential barrier, which the electrons have to pass, before reaching the detector. The large number of β-electrons from the source are emitted isotropically. The momentum p of an electron emitted with an angle of θ relative to the magnetic fields in the source can be split into a longitudinal component, which means parallel to the magnetic field lines and a transverse component, perpendicular to them. The kinetic energy of an electron is then split into longitudinal and transverse components:

$$E_{kin} = \frac{p^2}{2m} = E_\parallel + E_\perp \tag{2.1}$$

Due to the Lorentz force, the transverse component of the momentum is causing a cyclotron motion, while the longitudinal is responsible for propagation along the guiding magnetic field line through the beamline.

In order to scan the endpoint of the β-decay a retarding potential barrier qU_0 is used to prevent electrons with energies lower than the potential $E_\parallel < |qU_0|$ from reaching the detector. For this purpose a voltage U_0 is applied to the spectrometer vessel to induce an electric field $\vec{\epsilon}$ parallel to the magnetic field lines. Only electrons with $E_\parallel > |qU_0|$ can overcome the potential barrier in the central of the spectrometer and then be guided to
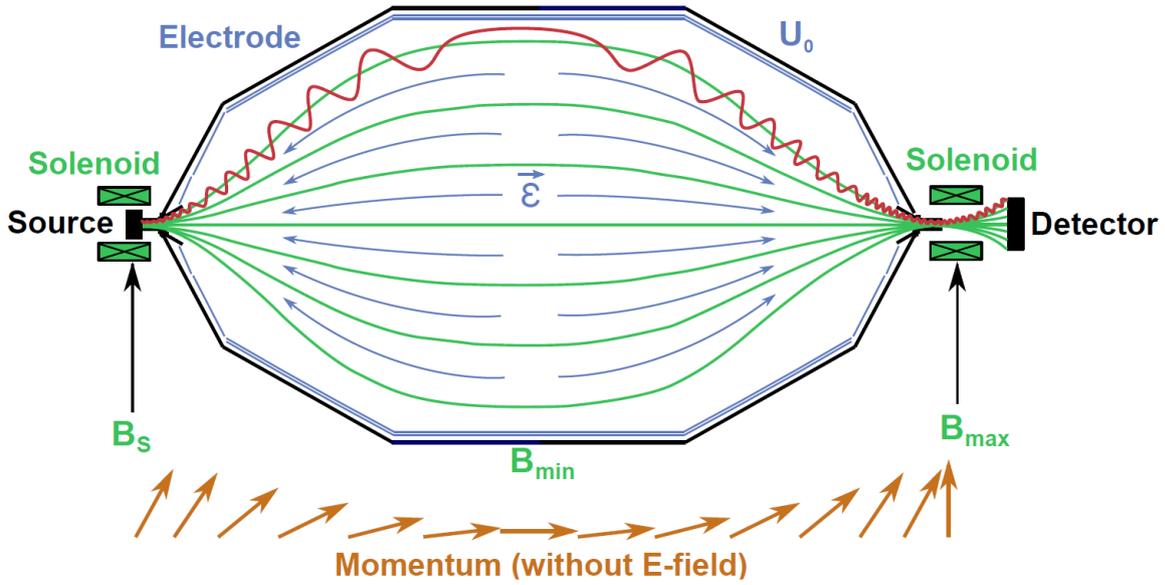
Figure 2.1: **Illustration of the MAC-E filter principle**. In the source on the left, β-electrons from tritium decay are emitted isotropically. Two superconducting magnets on the upstream and downstream end of the spectrometer provide a guiding magnetic field for the electrons. The electrons trajectories are shown in red and follow the green magnetic field lines superimposed by their cyclotron motion. A slow compared to the cyclotron motion of the electrons change in the magnetic field strength causes a adiabatic transformation of the transversal into longitudinal momentum shown in orange. At the maximum longitudinal momentum, respective lowest magnetic field, the retarding potential, shown in blue, filters the electrons with $E_\parallel < |qU_0|$. Electrons, which overcome the potential barrier leave the spectrometer on the downstream side and are counted by an electron detector. Figure adapted from: [38].

the detector system. By stepping the retarding voltage U_0 an integrated β-spectrum can be scanned. Since the electrons have a perpendicular momentum relative to the field lines, this component is not affected by the potential barrier. To prevent this, a adiabatic collimation of this momentum into longitudinal direction is indispensable. In order to guarantee adiabacity the field strength gradient along the electrons trajectory has to be small enough. The magnetic moment has to fulfill the following condition for a adiabatic scenario:

$$\mu = \frac{E_\perp}{B} = \text{const.} \qquad (2.2)$$

If the adiabacity is guaranteed, the electron's transversal momentum will transform into longitudinal momentum with decreasing magnetic field strength. Depending on the ratio of the minimum and maximum magnetic field strength nearly all of the electron's kinetic energy is transformed into longitudinal and consequently filtered by the retarding potential qU_0 in the point of minimum magnetic field strength, the analyzing plane. Since the transversal momentum is never transformed completely into longitudinal, the KATRIN
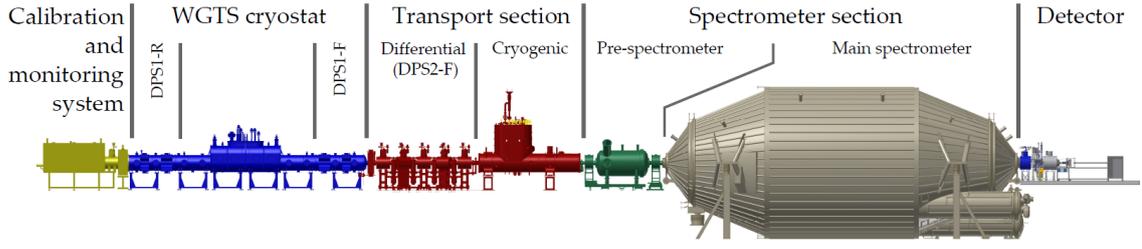
Figure 2.2: **Overview of the KATRIN beamline.** The 70-m long beamline houses several subsystems: The calibration and monitoring system monitors the activity in the **W**indowless **G**aseous **T**ritium **S**ource cryostat, where the β-electrons are emitted. The transport section provides an adiabatic transport of the electrons to the Spectrometer section, where the electrons are filtered by two spectrometers. If the electrons overcome the retarding potential they are counted by the electron detector at the downstream end of the beamline. Figure adapted from: [40].

spectrometer has a limited energy resolution:

$$\Delta E = \frac{B_{min}}{B_{max}} \cdot E_{kin} \tag{2.3}$$

With an endpoint energy of $E = 18.6\,\text{keV}$, an analyzing magnetic field strength of $B_{min} = 3 \times 10^{-4}\,\text{T}$ and a maximal field strength of $B_{max} = 6\,\text{T}$ one get an energy resolution of $\Delta E = 0.93\,\text{eV}$ [39].

One effect of high drops in the magnetic field strength is the magnetic mirror effect, where electrons are reflected when guided from a weak into a strong magnetic field. The maximum angle of an electron coming from the source not to be reflected is given by:

$$\theta_{max} = \arcsin\left(\sqrt{\frac{B_S}{B_{max}}}\right) \tag{2.4}$$

With $B_S = 3.6\,\text{T}$ and $B_{max} = 6\,\text{T}$ one gets $\theta_{max} = 50.77°$ for the maximum accepted starting angle of an electron.

The flux of a magnetic field is given by:

$$\Phi = \int_A \vec{B} \cdot d\vec{A} = const. \tag{2.5}$$

This yields to a higher diameter of the magnetic flux tube with lower magnetic field. At the two solenoid magnets the tube is reduced to a narrow beam, while in the analysing plane the flux tube reaches its maximum. The maximum diameter of the analyzing plane is then dependent of the source field B_S and its diameter d_s:

$$d_{AP} = d_s \cdot \sqrt{\frac{B_S}{B_{min}}} \tag{2.6}$$
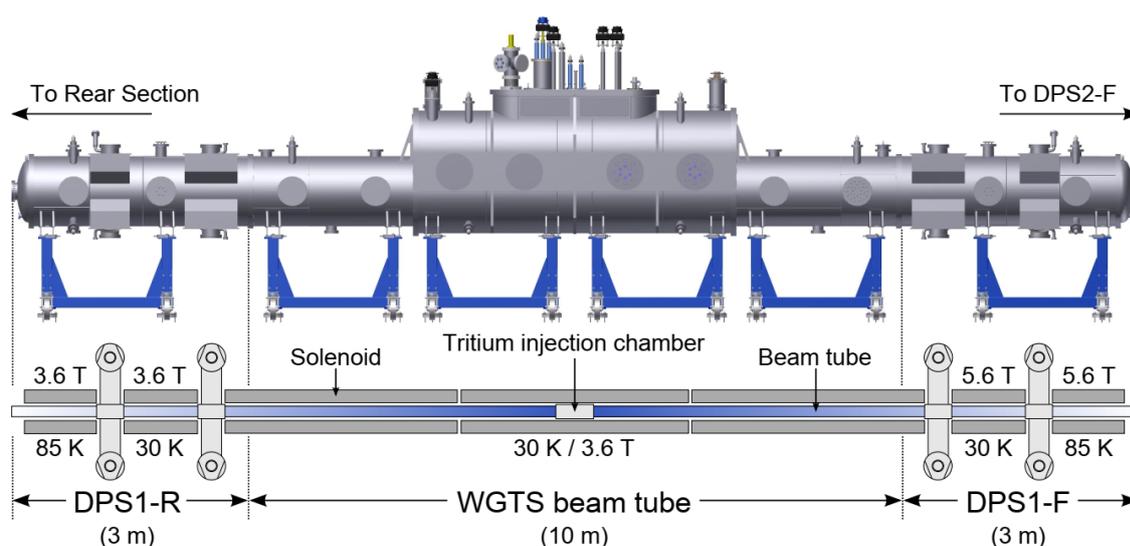
Figure 2.3: **Illustration of the windowless gasoues tritium source** with its 10m long stainless steel tube hold on a temperature of 30 K. In the center molecular tritium is injected with a tritium purity > 95 %. On the left and right two differential pumping section (DPS-I-R and DPS-I-F) are located in order to pump out tritium and other gases to avoid them reaching the spectrometer. Superconducting solenoids guide the β-electrons either to the transport section or to the rear section. Figure adapted from: [41].

This correlation is responsible for the dimensions of the spectrometer with a length of 23.6 m and a diameter of 10 m.

2.2 Experimental setup

With a beamline length of about 70 m the KATRIN experiment houses several components and subsystems shown in Figure 2.2. The β-electrons are emitted in the windowless gaseous tritium source, which provides a high luminosity with a high purity and stability, shown in 2.2.1. The β-electrons are magnetically guided through the transport section, shown in Section 2.2.2, where the rate of tritium is decreased by 14 orders of magnitude via turbo molecular pumps and cryosorption. In the spectrometer section shown in Section 2.2.3 the electrons are filtered with a system of two spectrometers using the MAC-E filter principle via a retarding potential. If the electrons have overcome that potential they are guided on a silicon wafer mounted in a detector system, described in Section 2.2.4, where they are detected.

2.2.1 Windowless Gaseous Tritium Source

The windowless gaseous tritium source (WGTS), shown in Figure 2.3 provides a tritium source with high luminosity and great stability. Gaseous molecular tritium is injected into the 10 m long stainless steel tube with a diameter of 9 cm via a set of capillaries with an

injection pressure of about 3×10^{-3} mbar. This prevents turbulences and guarantees a highly stable injection rate. The injected tritium then decays, by emitting an electron and an electron antineutrino:

$$^{3}_{1}\text{H} \rightarrow {}^{3}_{2}\text{He} + e^{-} + \bar{\nu}_{e} \tag{2.7}$$

In order to provide a column density of $\rho d = 5 \times 10^{17}$ cm^{-1} at a stability of 0.1 % the tritium is cycled through the WGTS. For this purpose the tritium is pumped out via turbo-molecular pumps, purified and feed back to the injection over different loops and purification cycles [42]. To monitor the tritium purity of $\epsilon > 95$ % a system using Laser Raman spectroscopy (LARA) is constantly monitoring the gas composition. This ensures a stable activity of $A \approx 10^{11}$ Bq [42]. In order to minimize Doppler-broadening via thermal fluctuation and reduce the throughput of the tritium, a neon cooling system keeps the beamtube at a temperature of 30 K with a high stability of ± 3 mK [43]. On both sides of the WGTS turbo molecular pumps reduce the tritium flow by two orders of magnitude in order to prevent the β-electron from scattering with tritium molecules, respectively from losing energy. The pumped out tritium is then analyzed, purified and re-injected into the WGTS [44].

Seven superconducting magnets, surrounding the beam tube are guiding the β-electrons with an magnetic field strength of $B_S = 3.6$ T. The collimated flux tube rise an cross section of 229 T cm^2, but only 191 T cm^2 are used for analysis due to possible scattering at the wall of the beam tube.

The Rear Section, located on the upstream side of the WGTS, provides controlling and monitoring of the WGTS. It allows to define the plasma potential, monitor the activity of the source by β-induced X-ray spectroscopy (BIXS) and measure the column density of the source [42].

2.2.2 Transport section

The β-electrons from the source are guided from the WGTS to the Spectrometer via the 14 m long transport section. The main task of the transport section is to reduce the tritium flow by 14 orders of magnitude, while guiding the β-electrons adiabatically. Additionally the tritium ions are removed. An inflow of tritium molecules into the spectrometer section would induce a increase of background. For this purpose the transport section consists of two subsystems: The differential pumping section (DPS) and the cryogenic pumping section (CPS).

While the DPS1-F, shown on the right side Figure 2.3, reduces the tritium flow by two orders of magnitude, the DPS2-F shown in Figure 2.4 (left) reduces the flow by another 5 orders of magnitude. A system of four large turbo molecular pumps housed in pump ports between five superconducting solenoids and two additional turbo molecular pumps up- and downstream reduce the flow, while the solenoids guide the β-electrons adiabatically to the spectrometer section. In order to prevent the molecular beaming effect, where
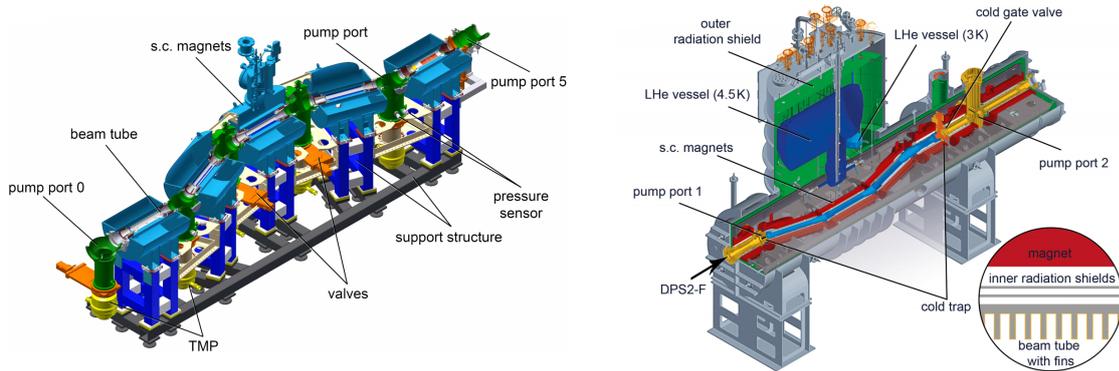
Figure 2.4: **Illustration of the KATRIN transport section. Left: Differential Pumping Section (DPS)** with its five superconducting solenoids (blue) guiding the electrons through two chicanes. Six pump ports (green), valves (yellow) and six turbo molecular pumps (yellow) reduce the tritium gas flow by seven orders of magnitude. The two chicanes prevent molecules from flowing in a direct line into the spectrometer.
left: Cryogenic pumping section (CPS) with the gold plated beam tube, surrounded by superconducting solenoids (red) guiding the β-electron through another two chicanes. The liquid helium vessel (dark blue) with reservoir for 4.5 K helium cool down the gold plated beam tube, where tritium is absorbed by argon frost, reducing the tritium flow by another 7 orders of magnitude. Figure adapted from: [45].

molecules could flow in a direct line into the spectrometer, the solenoids are tilted at an angle of 20°, leading to a chicane in the beamline. Additionally is the pumping efficiency of the turbo molecular pumps increased due to the chicanes. The solenoids can provide a magnetic field of $B_{CPS} = 5.6$ T and guide the electrons through the two chicanes, which are shown on the left side in Figure 2.4 [46].

To prevent ions from reaching the spectrometer different subsystems are installed in the DPS for ion identification and extraction. Ring-shaped electrodes with an applied voltage of up to +200 V block positive ions. A Fourier Transform Ion Cyclotron Resonance (FT-ICR) unit catches ions in a Penning trap and measures their cyclotron frequency for identification [47] [48]. Ion removal is provided by dipole electrodes, deflecting the ions on the walls of the beam tube via a $\vec{E} \times \vec{B}$ drift [49] [50].

In order to reduce the tritium flow even more, the Cryogenic Pumping Section is located between the spectrometer section and the DPS [51]. The CPS shown in Figure 2.4 uses the principle of cryosorption, the adsorption of tritium gas on argon frost. For this purpose liquid helium is used to produce an argon frost layer on the inner surface of the beam tube. With a reservoir containing liquid helium the beam tube is cooled down to a temperature of 3 K. Every 60 days the CPS is regenerated and the accumulated tritium is fed back into the tritium system. In order to regenerate the system it has to be warmed up to a tempterature of 100 K and flushed with helium gas. After that a new argon layer is

applied. In order to prevent molecular beaming the beam tube is tilted like in the DPS, by an angle of 15°. Additionally the tilted beam tube increases the trapping efficiency of the cryosorption. This system provides an additional tritium flow reduction in the order of 7 magnitudes adding up to a total of 14 orders of magnitude from the WGTS to the spectrometer section.

2.2.3 Spectrometer

The KATRIN experiment uses two spectrometers with the MAC-E filter principle to analyze the tritium spectrum near the endpoint: the pre-spectrometer, where the β-electrons are pre-filtered and the main spectrometer where the integral spectrum of tritium is measured. Both are operated due to background minimization at a pressure in the ultra high vacuum (UHV) regime in the order of 10^{-11} mbar. The low pressure also reduces the probability of scattering and therefore energy loss of β-electrons on their way to the detector.

The pre-spectrometer (PS) consists of a vacuum-vessel with 3.4 m length and 1.7 m diameter. Two superconducting solenoids (PS1 and PS2) provide the magnetic field of 4.5 T at both ends of the pre-spectrometer. The inner electrodes are set on a retarding potential of -18.3 keV to pre-filter the electrons with a reduction of flux by a factor of 10^7. This decreases the background due to scattered β-electrons with residual gas.

After passing the pre-spectrometer the β-electrons reach the main spectrometer (MS). With a length of 23.6 m and a diameter of 10 m its dimensions were a challenge from a technical, engineering and logistical point of view. The magnetic field is provided by the PS2 magnet, shared with the pre-spectrometer on the upstream side and the pinch magnet on the downstream side providing the highest magnetic field strength in the KATRIN beamline with $B_{PCH} = 6$ T. As shown in Section 2.1, in this setting the main spectrometer, acting as a MAC-E filter can provide a energy resolution of $\Delta E = 0.93$ eV. In order to fine-tune the magnetic field in the analyzing plane the main spectrometer is surrounded by air coils. This low field coil system (LFCS) consists of 14 normal conductive coils, which shape the magnetic field. With its 16 vertical and 10 horizontal air coils the earth magnetic compensation system (EMCS) compensated the non-axially symmetric earth magnetic field. An inner electrode system is used to fine-tune the electric retarding field inside the spectrometer. It consists of 24000 wires with a diameter of $200 - 300$ µm, mounted on 148 wire-electrode modules, which are arranged in a two layer design. In addition the inner electrode system is used to shield low energy secondary electrons emitted from the inner surface of the vessel by cosmic rays, intrinsic or environmental radiation or via field electron emission.

2.2.4 Focal Plane Detector System

The Focal-Plane Detector system (FPD) shown in Figure 2.5 is located downstream of the main spectrometer. Electrons which overcame the retarding potential of the spectrometer are guided onto the detector wafer in order to count them. The core of the detector system is a 148-pixel PIN diode, housed on silicon wafer. A detailed overview of the KATRIN
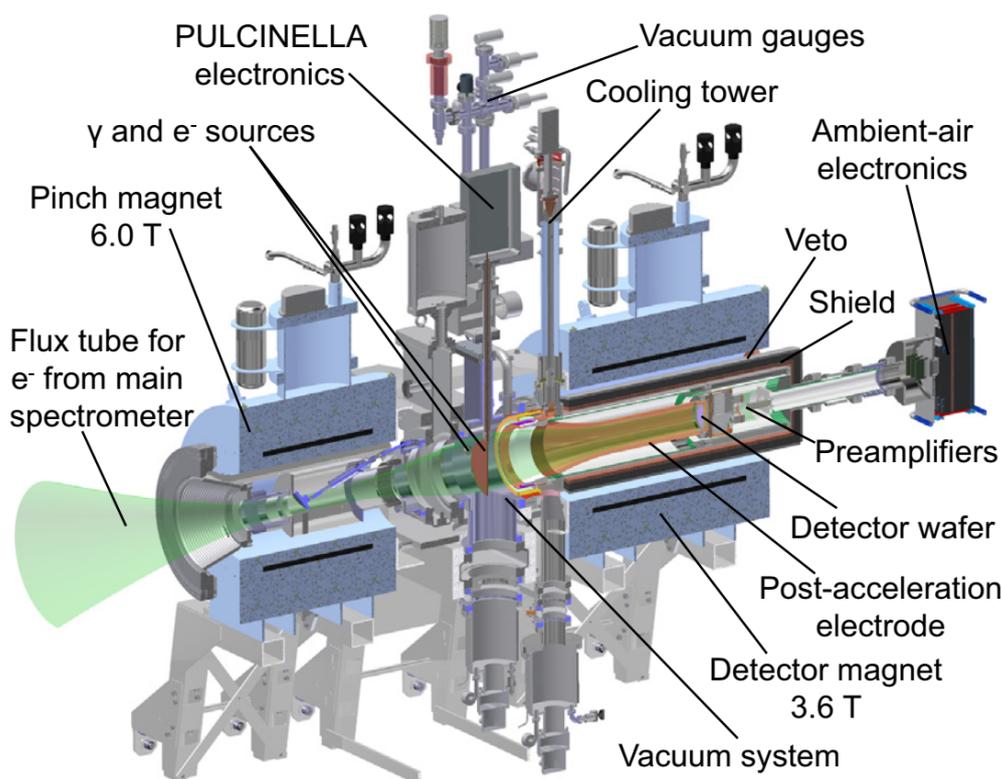
Figure 2.5: **Illustration of the Focal Plane Detector system** with its magnets, cooling and vacuum system, calibration sources and read out electronics. The electrons from the main spectrometer are guided by the Pinch magnet and the Detector magnet to the Post-acceleration, where they were boosted and then counted by the detector wafer. Figure adapted from: [52].

silicon wafer is given in Section 3.1

To guide the electrons onto the wafer a magnetic field is provided by two warm-bore superconducting solenoids. The pinch magnet, located directly on the downstream end of the main spectrometer with a magnetic field of $B_{PCH} = 6\,$T and the detector magnet, which surrounds the detector wafer, with a nominal magnetic field of $B = 3.6\,$T. The magnetic flux tube with those nominal fields is given by $210\,$T cm^2. Since the pinch magnet is run with higher magnetic field strength backscattered electrons from the detector are prevented from entering the main spectrometer and causing additional background. Both magnets are cooled down, to reach the superconducting state with liquid helium to a temperature of $T = 4.2\,$K.

The full copper trumpet-shaped Post-acceleration electrode shown in Figure 2.5 allows to accelerate the β-electrons up to additional $10\,$keV. Shifting the energy to higher values improves the signal to background ratio. Additionally the backscattering probability of the β-electrons is lower due to the decreased incident angle. Since the Focal Plane Detector system is directly connected to the main spectrometer it is in the ultra high vacuum regime
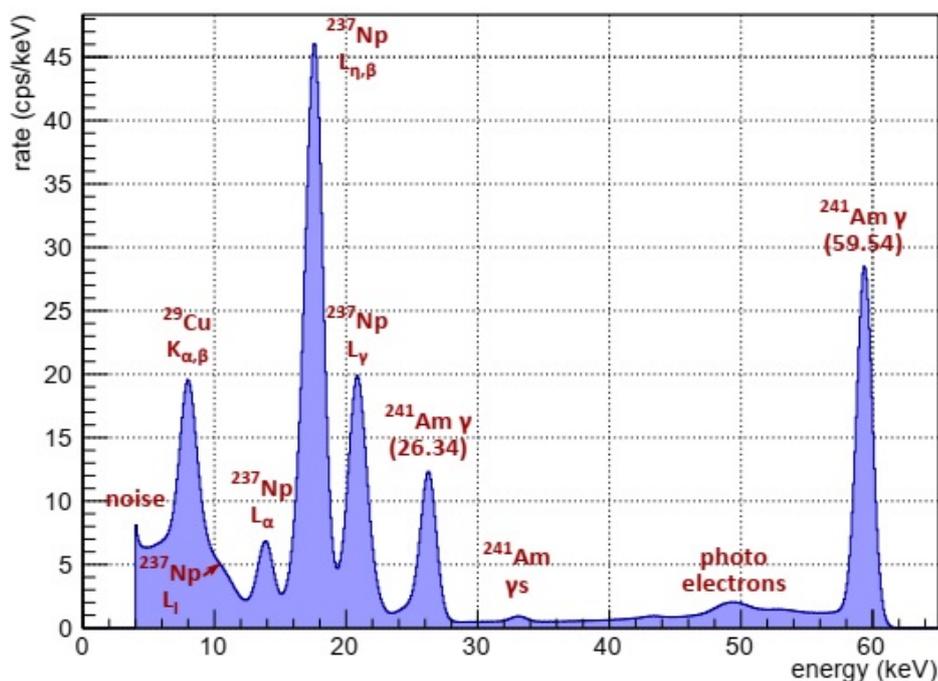
Figure 2.6: **The** ^{241}Am **spectrum** with the two γ-peaks at 26.34 keV and 59.54 keV, which are used for calibration. Additionally copper fluorescence lines due to the post-acceleration electrode, X-ray lines of ^{337}Np and photo electrons are shown. Figure adapted from: [52].

at about 10^{-11} mbar. The Post-acceleration electrode seperates the ultra high vacuum from the high vacuum, where the front-end electronics of the detector system is located.

In order to read out the signals from the detector wafer diverse readout electronics is installed. A detailed overview of the readout electronic and the data acquisition of the Focal Plane Detector system is given in Section 3.3.2. Due to the heat produced by the electronics an active cooling is needed. For this purpose a custum made heat pipe has been developed and installed in the FPD system. To cool down the detector system it is mounted on the Post-acceleration electrode. Cooling down the detector system improves the energy resolution of the wafer due to lower noise. This behaviour is investigated in Section 3.4.

In order to calibrate the FPD system it provides several sources of calibration. Mono-energetic γ-photons of a ^{241}Am-source are used to calibrate the FPD system. Therefore two peaks in the γ-spectrum as shown in Figure 2.6, one at 26.34 keV and another at 59.54 keV are used to calibrate the system via a linear regression. Additionally it is possible to use photoelectrons produces via an UV-illuminated titanium disc for calibration. In contrast to the γs the photoelectrons lose energy in the detectors dead layer. Using the calibration source and the peak width of the γ-spectrum a determination of the energy resolution is

possible. The performance of the Focal Plane Detector system has been investigated in Section 3.4.

3 Characterization of the KATRIN silicon wafers with the Iron Bird test setup

The KATRIN Focal Plane Detector System counts the electrons, which overcome the retarding potential in the MAC-E filter. It has to detect electrons from tritium β-decay with energies up to 18.6 keV, conversion electrons from ^{83}Kr with energies from 17.8 keV up to 32 keV and electrons from a high rate electron gun highly efficient and with a good energy resolution. Additionally the detector has to be position sensitive in order to investigate spatial effects like inhomogeneities in the analyzing plane or suppression of background coming from outside of the magnetic flux tube [39].

All these properties are realized with a silicon PIN-diode described in Sec. 3.1. One attribute of the detector system is a good energy resolution. An investigation of the energy resolution of the KATRIN silicon wafers is shown in this Chapter.

During a SDS3c measurement in 2017 a major Penning discharge of the Penning trap located between the pre- and main spectrometer caused damage to the mounted wafer (#115878). In 2018 this wafer was replaced by a wafer, which is mounted in the FPD system (#96725) till now. In the KATRIN Neutrino Mass measurement phase (KNM1), which started in 2019 several pixels (97, 98, 110, 111, 121, 122) had to be excluded from the analysis due to a bad energy resolution. The fact, that the pixels are located in the same area, lead to the conclusion of a damaged area on the wafer. In order to guarantee a working detector system for future measurements it is considered to replace the currently installed wafer. Before mounting a wafer in the Focal Plane Detector System a number of tests have to be completed successfully.

Once a wafer arrives at the KIT several steps of characterization are performed with this wafer. In 2012 a wafer (#96728) with shorted pixels shown in Figure 3.1 was mounted in the FPD system. To avoid mounting faulty detector wafers in the system, a wafer test setup has been built up at by E. Martin (University of Washington) in 2014 [53] in order to test new wafers for shorted pixels. The setup of this test device is described in Section 3.2.

In the next step a characterization regarding the energy resolution and behaviour in a KATRIN-like detector and readout setup has to be performed. For this purpose a test setup, called Iron Bird, has been established to characterize the KATRIN wafers. This test setup is described in Section 3.3. The characterization of two wafers of a new batch with the Iron Bird test setup and a comparison with the recently mounted wafer is shown in Section 3.4.
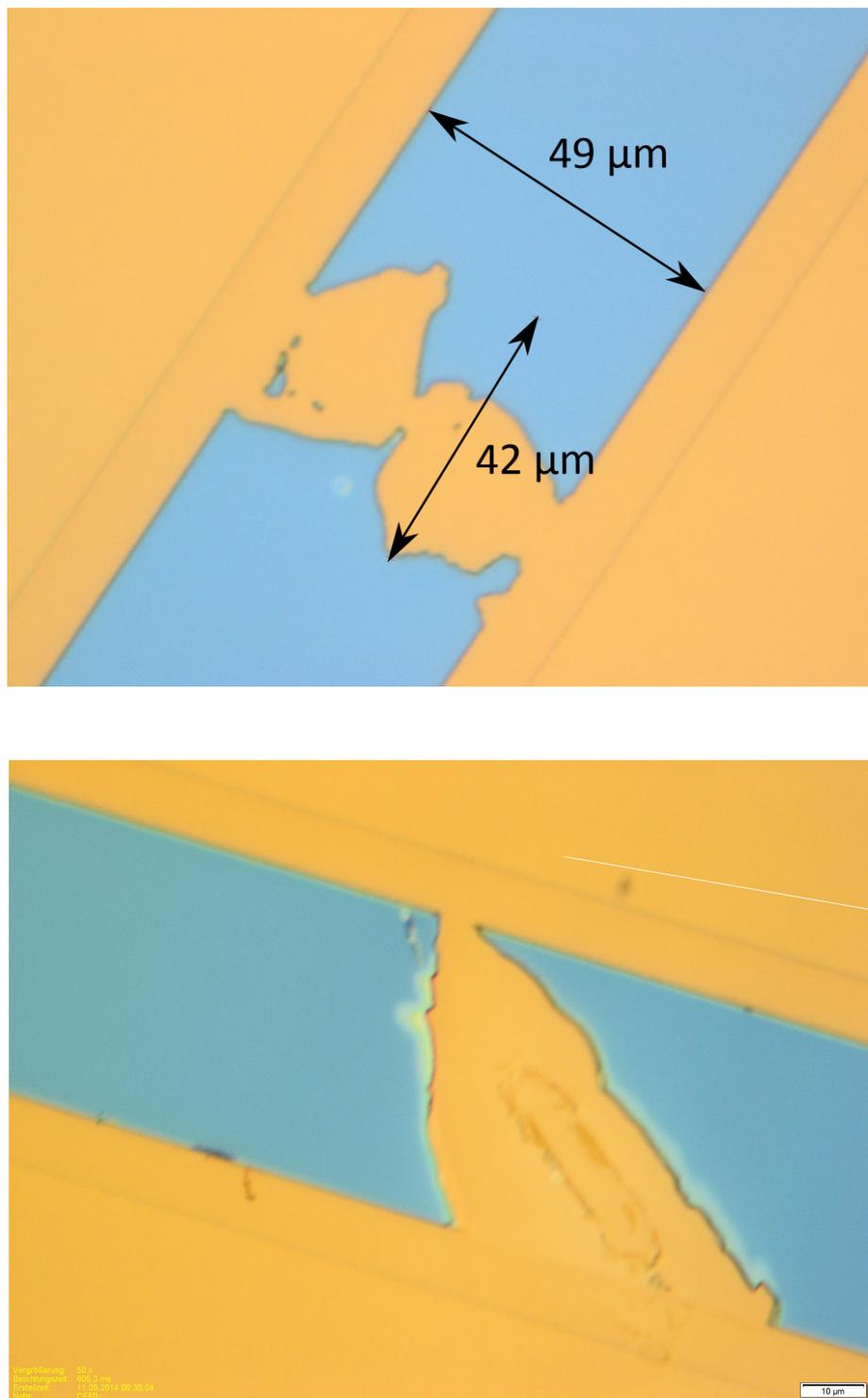
Figure 3.1: **top: Shorted pixels** of wafer #96728.
bottom: Shorted pixels of wafer #115874. Figure adapted from: [55].
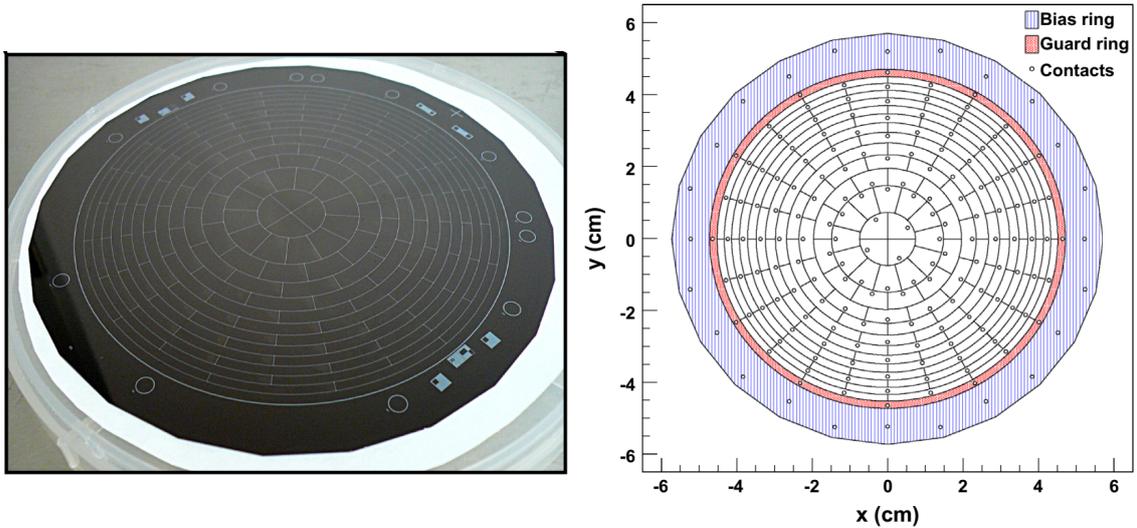
Figure 3.2: **left: Detector wafer** (backside) with its dart-board-like segmentation, 12 concentric rings with 12 pixels each and 4 bulls-eye pixels.
right: dartboard pixel pattern with electrical contacts, guard ring and bias ring. Figure adapted from: [52].

3.1 The KATRIN silicon wafers

To count the β-electrons in the Focal Plane Detector system a monolithic 148-pixel p-i-n-diode housed on a silicon wafer is used. This wafer is 125 mm in diameter and has a thickness of 503 µm. The entrance side of the wafer consists of an unsegmented, shallowly ion-implanted, n^{++} layer, which has a diameter of 90 mm. This sensitive window is surrounded by a 2 mm guard ring and a 15.5 mm bias ring. The thickness of the non-sensitive dead layer at the entrance has been determined to be $155.4 \pm 0.5 \pm 0.2$ nm [54]. The ion-implanted p-type contact side at the back of the wafer is completely coated with non-oxidizing TiN to contact the pixels. To apply the bias voltage of $U_{bias} = 120$ V via the bias ring the TiN layer wraps around the edges of the wafer. Between the n^{++} and the p^- layer a mildly doped or intrinsic layer is located. To investigate spatial effects with the detector system the wafer is segmented on the backside into 148 pixels of equal area of 44.1 mm^2. The pixels are separated via 50 µm-boundaries with an pixel-to-pixel resistance larger than 1 GΩ and have a design capacitance of 8.2 pF. The segmentation, shown in Figure 3.2, consists of 4 bulls-eye pixels in the center and 12 concentric arranged rings of 12 pixels each. Since in 2012 a wafer with shorted pixels was mounted in the FPD system a test setup has been established to check a wafer for shorts and other parameters. This setup is shown in the next section.

3.2 Wafer test system

The Wafer test system consists of standoffs, the pin alignment section, the printed circuit board (PCB) with multiplexers and the top section for fixture. After the detector wafer is
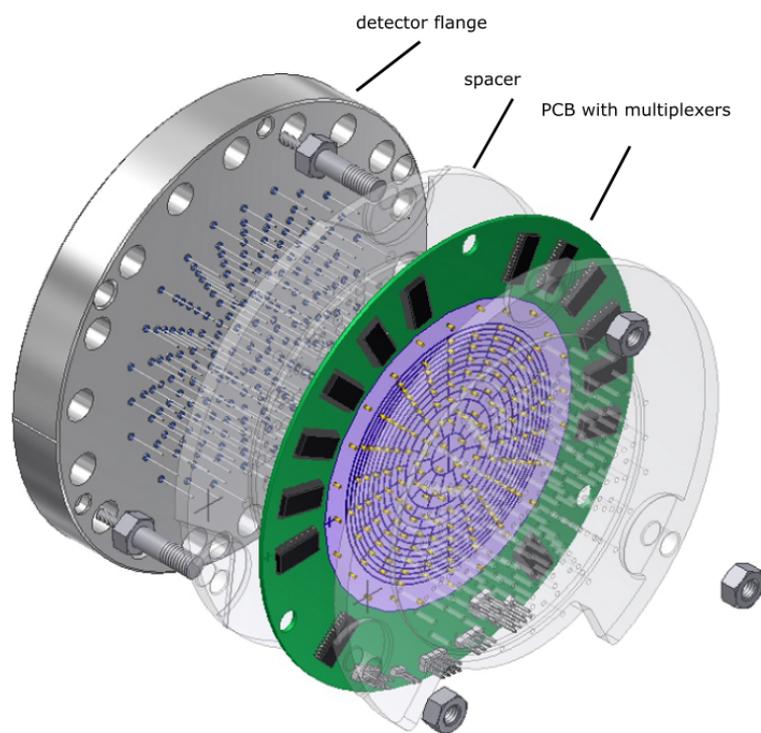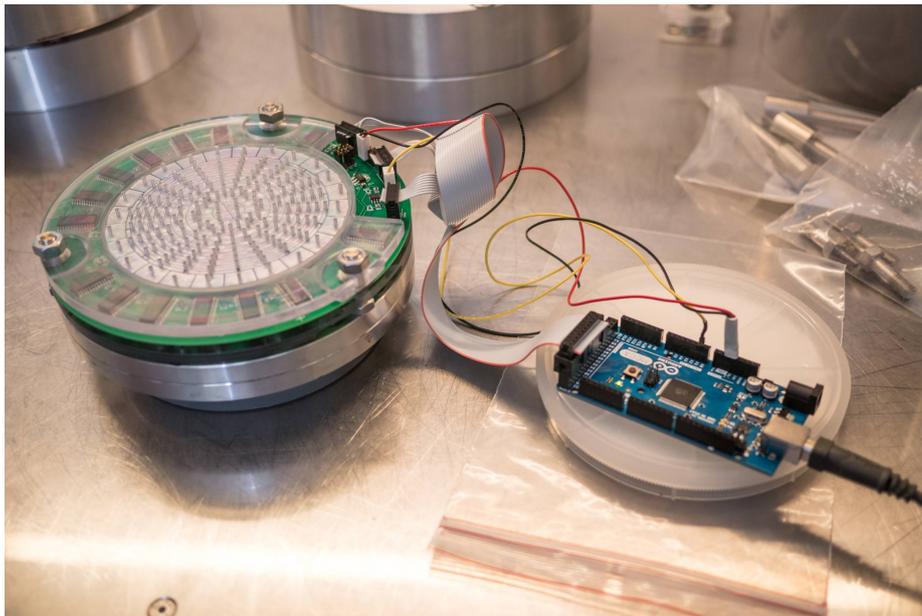
Figure 3.3: **top: Wafer test system** mounted on the detector flange.
bottom: Wafer test system with detector flange, spacer and printed circuit board (PCB) with multiplexers. Figure adapted from: [53].

installed on the feedthrough flange, it can easily be mounted on the Wafer test system. At first the pin alignment section is attached to make sure the pins are fixed in the right position. The PCB is separated from the feedthrough flange via a plastic spacer. To push the PCB with its readout contacts against the pogo pins, a second spacer is put on and mounted with nuts. The PCB uses 12 multiplexers with 16 channels for adressing the 184 sockets. A 13th multiplexer is used to adress the enable pins of the used multiplexers. To measure the resistance between two pixels, two sets of multiplexers allow two connections to each socket. With the first set of the multiplexers, a known test voltage is applied to an FPD socket, while the other set of multiplexers applies a known voltage through a known resistance to a socket. By measuring the voltage on the socket you can determine the voltage and resistance between the two pixels. All tests with this test system are controlled, powered and read out via an Arduino Mega 2560 over USB and the integrated Arduino IDE. Controlling is realized over a serial connection. The User can choose between the following measurements:

- Bias ring connection: This test checks, if the resistance between the bias ring pins is low enough.

- Guard ring connection: This test checks, if the resistance between the guard ring pins is low enough.

- Pixel-to-pixel shorts: To avoid shorts between two pixels, this test checks for a high enough resistance between adjacent pixels.

- Forward bias check: This test measures the forward bias from the pixels to the bias ring.

- Reverse bias check: This test checks, if the reverse bias resistance is good enough.

All parameters like number of iterations and minimum pixel-to-pixel resistance can be set by the user via the serial interface. All information regarding the Wafer test setup are taken from [53].

After arriving at KIT in 2019 the two wafers of the new batch were mounted on the Wafer test system to check them on shorts between pixels and other parameters. Both of the wafers passed the tests successfully.

3.3 Experimental setup of the Iron Bird test setup

Since the Iron Bird test setup was built to investigate the performance of the KATRIN silicon wafers it should behave like the KATRIN detector system regarding noise and background contributions. For this purpose parts like the Readout Electronics and Data Acquisition were designed equivalent to the KATRIN detector system.
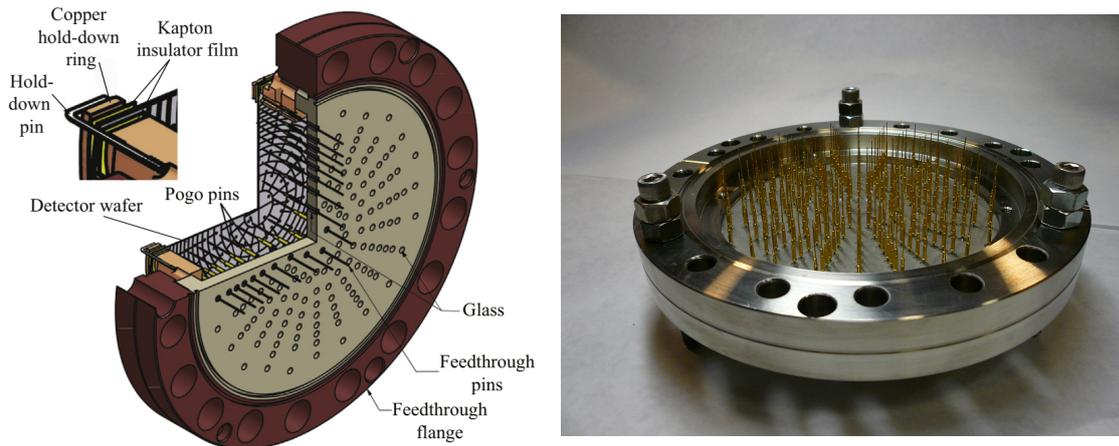
Figure 3.4: **left: Schematics of feedthrough flange** with detector wafer, pogo pins, hold-down rings and pins, connection pins, and eletrical feedthrough. Figure adapted from: [52].
right: Feedthrough flange with 184 spring loaded pogo pins.

3.3.1 Focal Plane Detector system

The Focal Plane Detector consists of the 148-pixel PIN diode described in Section 3.1, a mounting structure for the wafer and the vacuum electronics, which is described in Section 3.3.2. To guarantee an appropriate electrical contact, the wafer is mounted on a custom made feedtrough flange, as shown in Figure 3.4 (left) with a copper hold-down ring and six hold-down pins. Copper stops center the wafer on the feedthrough flange. The individual pixels are read out via gold-plated and spring-loaded Interconnect Devices pogo pins with a Ni-Ag barrel, Be-Cu plunger and a stainless-steel spring. To reach good electrical contact the required compression of each pin is at least 0.38 mm which adds up to a total force of 50 N pushing against the detector wafer. This yields to a deformation of the wafer in the center of 0.24 mm which has no noticeable influence on the detector performance.

3.3.2 Readout Electronics

To read out the detector signals a custom-made suite of electronics designed and manufactured by the Institute for Data Processing and Electronics (IPE) at KIT is used. The first stage of signal processing are 24 preamplifier modules which are directly mounted to the connection pins at the feedthrough flange to reduce noise. The carousel-like radial arrangement of the 24 modules is shown in Figure 3.5. Each module preamplificates either six or seven channels of the detector.
To withstand the high vacuum conditions and heat dissipation the modules are build on 0.63-mm-thick Rubalit 710S aluminum-oxide ceramic boards. To transport the dissipated heat of about 0.6 to 1 W per module, they are mounted with special copper mounting plates and pins (shown in Section 3.3.5). The modules are equipped with multiplexers, switching devices, decoders and current-to-voltage converter circuitry for test-pulsing
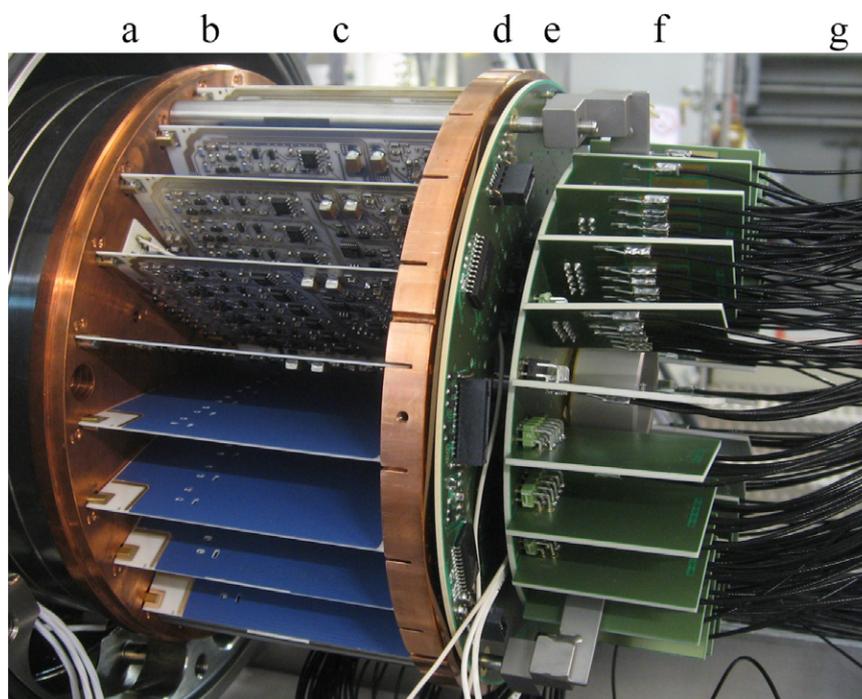
Figure 3.5: **Focal Plane Detector system** with feedthrough flange (a), copper mounting disc (b), preamplification cards (c), copper mouting ring (d), power and control ring board (e), signal distribution board (f) and cable harness (g). Figure adapted from: [55].

and also for leakage-current and temperature readout. Additionally the modules houses two noise-filtered feedthrough lines to supply the wafer with its guard-ring and bias voltage. A second ring-shaped distribution board is used for powering and controlling the preamplification modules. To distribute the preamplified signals to the cable harness, a circular signal distribution board is attached to the preamplification modules. The signals are then led out of vacuum via four 50-pin D-Sub feedthrough connectors to ambient air. There four 37-channel signal boards provide differential transceivers, additional amplification and variable-gain stages. Since the electronics is on the same voltage as the Post-acceleration electrode it has to be isolated from the data-acquisition system outside of the high voltage area. For this purpose the Optical Sender Boards convert the analog signal by fiber-optic transmitters into an optical signal in order to transmit them via plastic-optical-fibers to the data-acquisition system. Additionally a power-and-control board includes power-conditioning circuits, overvoltage protection, variable-gain controls and temperature readouts. The optical receiver boards with fiber-optical receivers convert the optical signals to analog signals for digitizing [52].

3.3.3 Data Acquisition

The Data Acquisition system is split into two subsystems, which are closely coupled: the DAQ electronics, shown in Figure 3.6 and the DAQ software.
While the analog systems are made specifically for KATRIN, the digitizers and digital
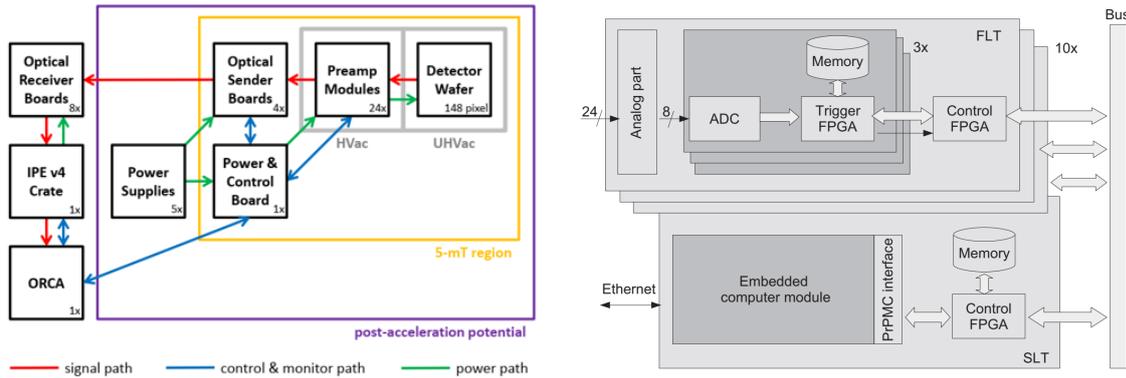
Figure 3.6: **left: Schematic overview of the read out and data acquisition** with signal path, control & monitor path and power path. Figure adapted from: [52].
right: Schematic architecture of the DAQ electronics with first level trigger and second level trigger. Figure adapted from: [52].

components are build rather universal. The digital shaping of the detector traces is accomplished via field programmable gate arrays (FPGA). This allows to set filter parameter, such as shaping length and gap length individually. The DAQ hardware uses the same design as used for the Pierre Auger Cosmic Ray Observatory: first-level trigger (FLT) and second-level trigger (SLT) cards. Both are mounted in the IPE v4 crate. Eight FLT cards, each handling up to 24 channels, are processing the detector signals using analog differential receivers with programmable offsets and amplifiers, bandpass filters, digitizer drivers, serial ADCs and auxiliary memory for the ADCs. The serial ADCs provide a 12-bit resolution and a sampling rate of 20 MHz. Each FLT card houses four Altera Cyclone II EP2C35 FPGAs, which allow flexible filtering and triggering. Three of the FPGAs are used for triggering (slaves) to control the data acquisition and preprocessing, while each can handle eight channels. One FPGA operates as central-control FPGA (master) for time synchronization and readout for each FLT card. After passing a two-stage filter the information is transmitted to the master FPGA, if the signal exceeded a programmable threshold. To initialize and coordinate the FLT cards one single SLT card, realized by a crate PC equipped with a 10-Gbit network card, is used. The communication between the SLT card and the DAQ computer is realized by a fast Ethernet interface, while the synchronization uses the network time protocol. Additionally a synchronization unit provides a high-precision 10-MHz signal as well as a 1-Hz signal for internal synchronization [52].

To record the ADC traces the DAQ electronics uses a circular ring buffer with 64 pages, each with 2048 samples and four bit-status indicators. The readout system has to handle a high range of event rates. While the rate during neutrino-mass measurements is expected to be less than 1 cps the system has to deal with rates up to 1 Mcps during calibration runs. To avoid dead time and loss of events due to high rates there are three different DAQ modes available, as you can see in Table 3.1. Since the energy mode records energy and timing of each event it is the primary data-taking mode and can handle up to 108 kcps per crate. For diagnostics the trace mode adds a 2048-bin digitized waveform of each event

DAQ mode	Trace	Energy	Histogram
ADC trace	x		
Event identifier	x	x	
Time stamp	x	x	
Energy	x	x	
Channel map	x	x	x
Trigger rate	x	x	x
Energy histogram			x
Event size	4 kB	12 B	
Histogram size			8 kB
Max. rate (deadtime-free)	8 kcps	108 kcps	3.3 Mcps

Table 3.1: **Data acquisition modes** with Trace, Energy and Histogram mode. Figure adapted from: [52].

but can record only up to 8 kcps. To guarantee a lossless data taking at very high rates the FLT hardware fills a 2048-bin histogram for each channel. Since the traces, time stamps and energies of each event are not recorded, an event-bases analysis is not available in histogram mode.

An electron hitting the detector causes a step-like response in the signal, where the step height is proportional to the electron's energy. This signal has a typical rise time of 200 ns and a fall time of about 1 ms. To detect these steps and determine the event's timing and energy two trapezoidal filters are applied. One filter stage is defined by its shaping length L and its gap length G, both in multiples of 50-ns ADC time bins. The filtered signal output for each time bin i is given by the difference of two moving sums over the previous $2L + G$ ADC bins v_i, where the time windows of the sum is given by L and the separation between those time windows is given by G:

$$S_i = \sum_{j=0}^{L} v_{i-j} - \sum_{k=L+G}^{2L+G} v_{i-k} \tag{3.1}$$

The maximum after the first filter occurs L times after the step and is equal to the step height. The gap length prevents the non-vanishing rise time from affecting the energy determination and results in a flat top of length G. The second filter with a shaping length of L/2 and no gap length is now applied on the signal output of the first filter. Now a maximum in the signal of the first filter corresponds to a zero-crossing after the second filter. If the maximum of the first filter exceeds a programmable energy threshold, the trigger releases. A large shaping length improves the energy resolution while a small shaping length optimizes the timing resolution. One waveform sample where both filters have been applied is shown in Figure 3.7.

Processing of the data is done via a DAQ software package called ORCA (Object-oriented Real-time Control and Acquisition) developed at the University of Washington and the University of North Carolina at Chapel Hill. It provides a graphical user interface, where all configurations can be done at run-time with no compilation. OrcaROOT than allows to analyze ORCA generated data using the ROOT software packages [52].
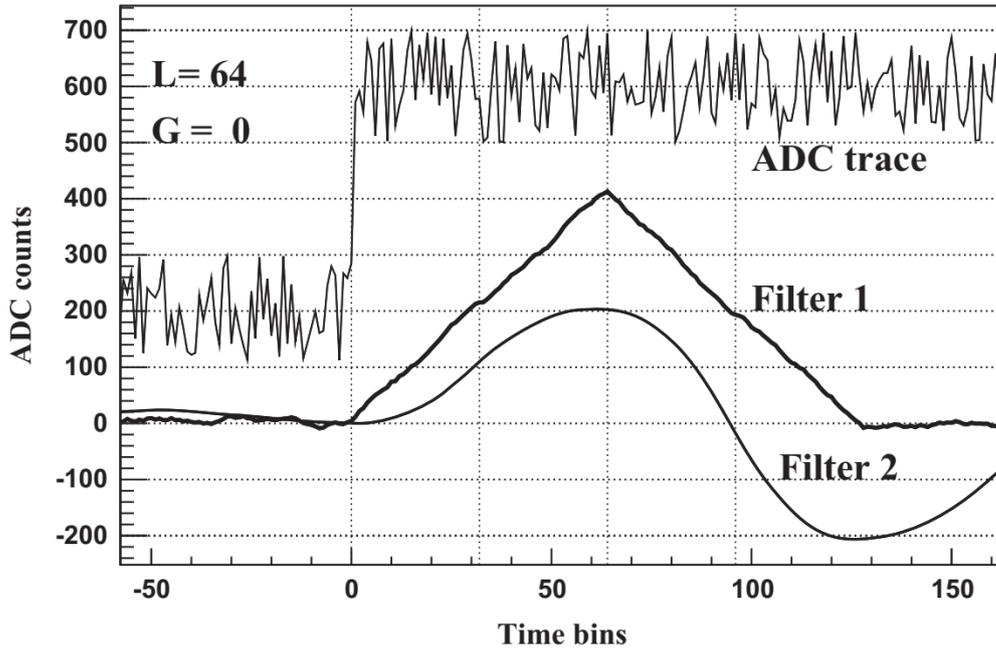
Figure 3.7: **Trapezoidal filter serias** with waveform sample, first and second trapezoidal filter. Figure adapted from: [52].

3.3.4 Vacuum Chamber

The Iron Bird Vacuum Chamber, shown in Figure 3.8 houses the detector system and its vacuum readout electronics. This includes the feedthrough flange where the wafer is mounted, the preamplification cards, the signal distribution board, power distribution board, cable harness and the 50-pin D-sub feedthrough. The Vacuum Chamber consists of a 97 cm long aluminum tube with a diameter of 25.4 cm and with vacuum flanges on both sides. Via a KF-25 pump port a Pfeiffer HiCube vacuum pump can be attached to evacuate the vacuum chamber 2×10^{-5} mbar. At one end of the Vacuum Chamber five 50-pin D-sub feedthroughs lead out the signals from the vacuum to the ambient air electronics and provide the supply voltage of the power-anc-control and signal distribution board, the amplification cards and the detector.

3.3.5 Cooling system

In order to prevent overheating and for noise reduction the detector and its vacuum electronics requires an active cooling. For this purpose a CP-110 Peltier-Thermoelectric Cold Plate Cooler from TE Technology, Inc. can be attached to a copper plate at one side of the Vacuum Chamber, shown in Figure 3.15. To avoid condensation on that plate, a hermetically sealed chamber encloses the cold plate, as seen in Figure 3.9. The vacuum system contains the detector, the preamp cards, the power-and-control and the signal distribution board. This whole system is spring-loaded on four support posts to improve the thermal contact between the detector feedthrough flange and the cold plate. The
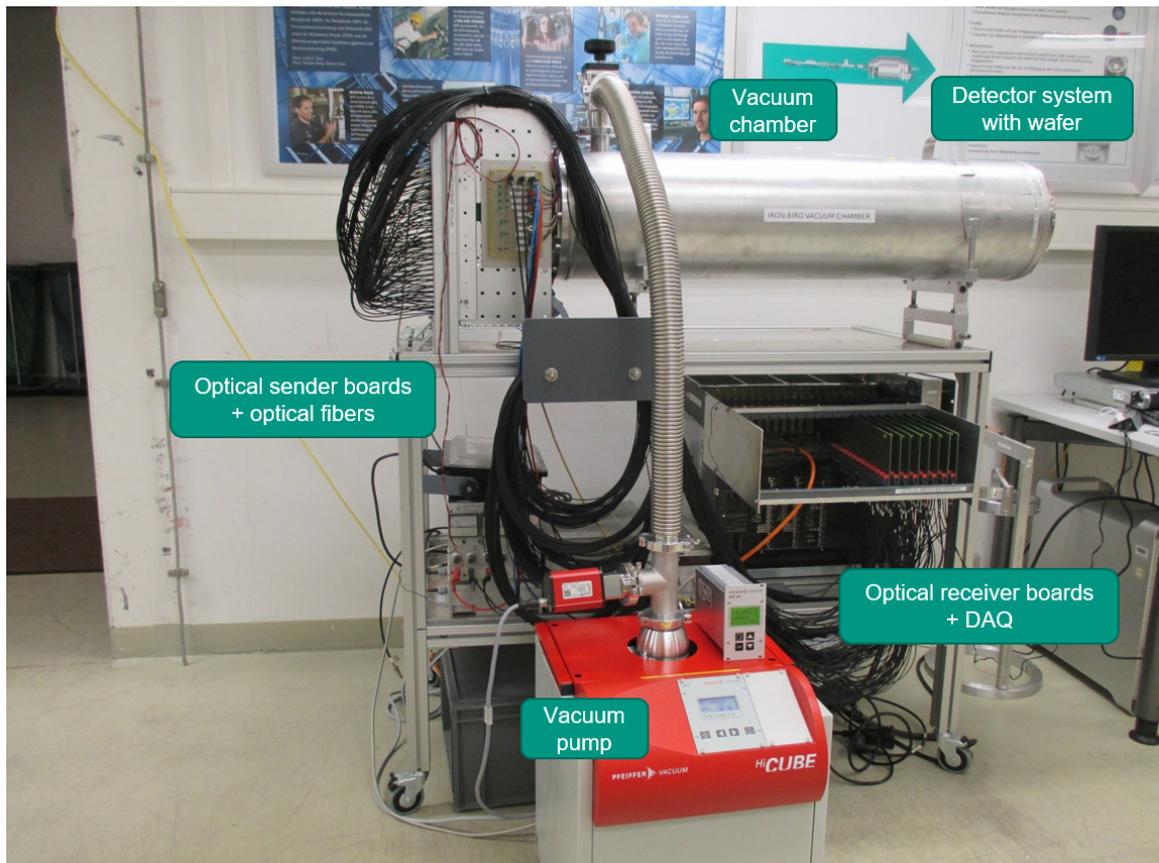
Figure 3.8: **Iron Bird test setup** with detector system, vacuum chamber, optical sender and receiver boards, on DAQ table, with attached vacuum pump

detector flange is then attached to a copper disc where the 24 preamplification cards are mounted with special copper pins to conduct the heat. The measured heat dissipation of one of the modules is 0.72 W. This yields to a dissipated heat of 4.32 W per quadrant and 17.28 W in total [55].

The CP-110 peltier cooler provides a direct-contact cooling, with integrated PID-loop for temperature regulation [56]. The cold plate of the cooler can be attached and fixed with four bolts to the cooper cooling plate. With an ambient air temperature in the range of 14 to 20 °C and a setpoint of the cooling plate of −15 °C the maximum cooling power is approximately 25 W. Assuming a total heat dissipation of 17.28 W of the detector system an active cooling should be possible. To investigate the cooling behaviour several Pt-100 sensors were connected to the detector system. To examine the thermal connection between the copper cooling plate and the detector feedthrough flange one sensor was attached to the flange. Additionally two sensors were attached to the copper mounting plate where the preamplification boards are mounted as well as to the copper support ring, shown in Figure 3.5. In Figure 3.11 a cool-down cycle is shown. The setpoint of the peltier cooler was set to −15 °C. After running the cooling for 18 hours the temperatures in the thermal equilibrium are shown in Table 3.12. The difference between the peltier cooling
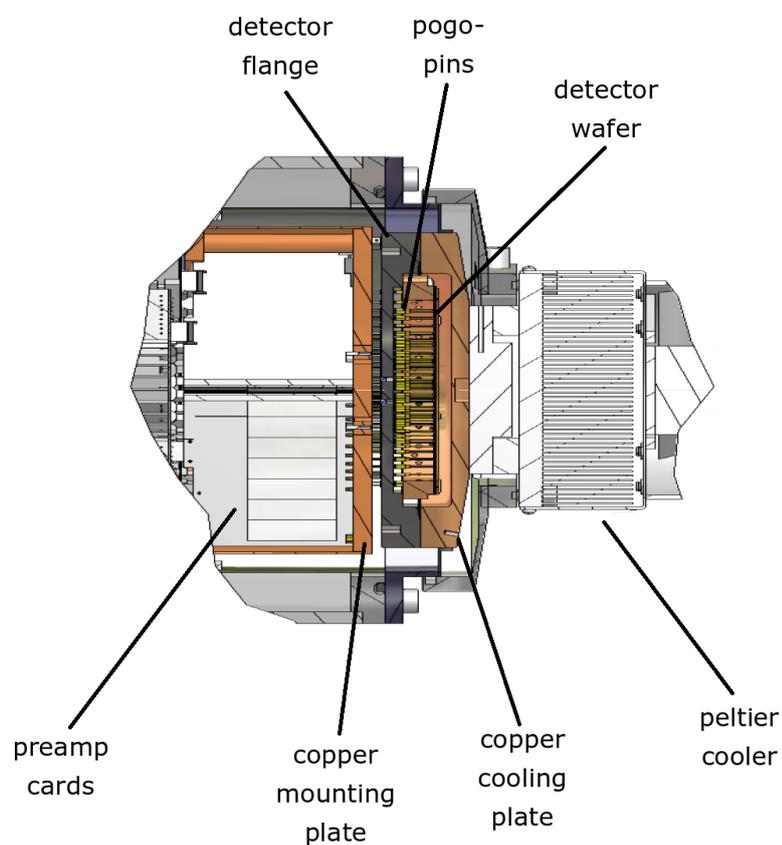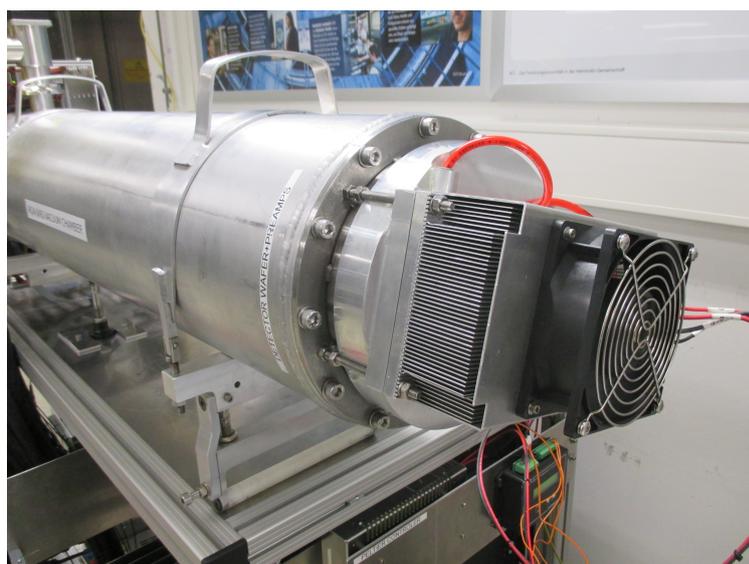
Figure 3.9: **top: Peltier cooler** with hermetically sealed enclosure, attached on Iron Bird vacuum flange.
bottom: Technical drawing of the detector system inside the Iron Bird vacuum chamber.
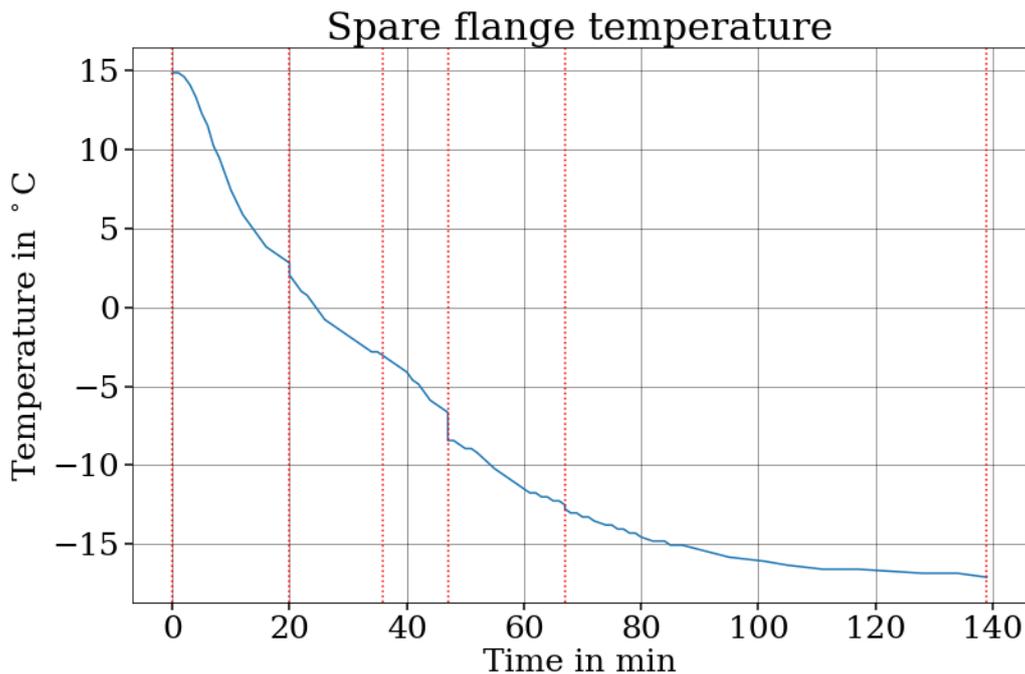
Figure 3.10: **Temperature measurement with Pt-100 sensors and detector spare flange** at different peltier setpoint: $0\,°C$, $-5\,°C$, $-10\,°C$, $-15\,°C$ and $-20\,°C$. While changing the setpoint (red dashed lines) of the peltier cooler, the measurement was stopped. The continuing cooling during these stops caused the steps in the plot.

plate and the detector flange amounts $12.9\,°C$. The correlation between the detector flange, copper mounting disc and copper support ring lead to the conclusion, that the thermal coupling of the detector system is existent unlike the thermal connection between the peltier cooling plate and the detector flange.

To investigate the thermal contact between the detector system and the copper cooling plate a test setup was arranged with a detector spare flange. No wafer or electronics are mounted on that flange. In the test setup as shown in Figure 3.13 the peltier element was fixed to the copper cooling plate which is embedded into the vacuum flange. This assembly was fit on top of the spare flange. To prevent condensing of water on the flange it was put on a foam mat. Two Pt-100 temperature sensore were used for temperature readout both directly on the spare flange and on the outer side of the vacuum flange. At first the peltier cooler setpoint was adjusted to $0\,°C$ and then lowered after the slope did not change significantly in steps of $5\,°C$. At the last setpoint of $-20\,°C$ the temperature of the copper cooling plate reached a minimum at $T = -18.8\,°C$ with an power output of the peltier element of $100\,\%$. The temperature of the spare flange in thermal equilibrium was $T = -17.1\,°C$, while the temperature of the vacuum flange was $3.57\,°C$. This yields to a temperature difference of $1.7\,°C$ and the conclusion, that in that specific setup with the
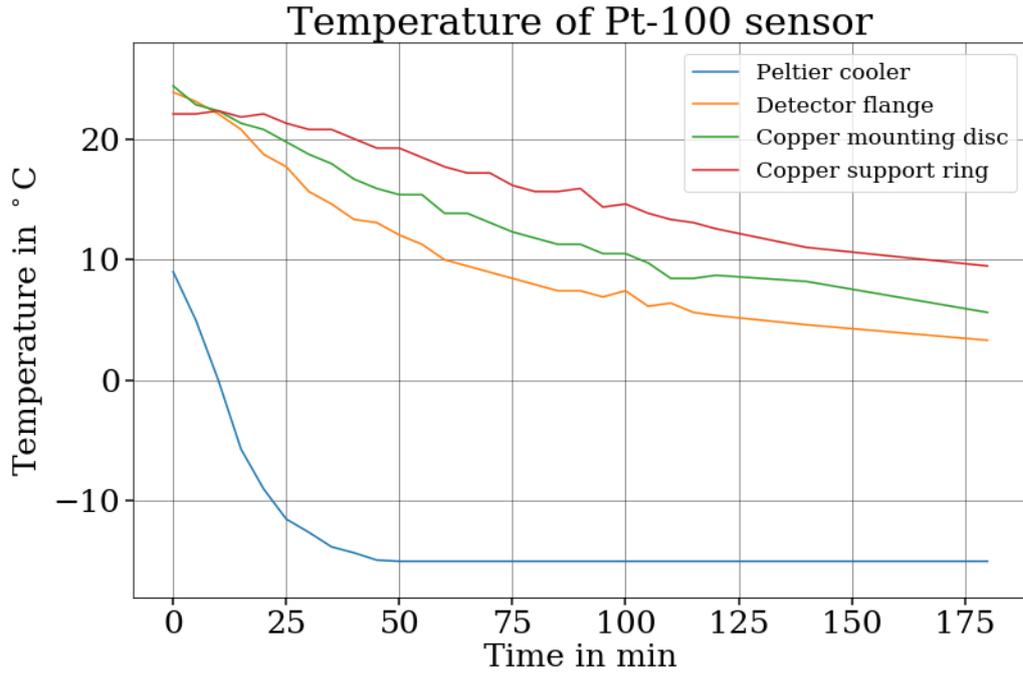
Figure 3.11: **Temperature measurement with Pt-100 sensors** attached on different locations: On the peltier cooler, detector flange, copper mounting disc and copper support ring.

Peltier cooler	Detector flange	Copper mounting plate	Copper support ring
$-15\,°C$	$-2.06\,°C$	$0.25\,°C$	$4.1\,°C$

Figure 3.12: **Temperatures in thermal equilibrium** after 18 hours of cooling.

spare flange and no thermal load the thermal contact between the surfaces of the cooling plate and the detector spare flange conduct the heat sufficiently.

The rate of heat flow of the detector system radiating to the vacuum chamber can be calculated via the Stephan-Boltzmann law, assuming the radiant surface of the detector system to be much smaller than the surrounding surface of the vacuum chamber:

$$\dot{Q} = \epsilon\sigma A(T_1^4 - T_2^4) = 6.6\,\text{W} \tag{3.2}$$

where $\epsilon = 0.76$: emissivities of the Cu-surface, σ: Stefan-Boltzmann constant, $A = 520\,\text{cm}^2$: surface area, $T_1 = -15\,°C$: temperature of the detector system, $T_2 = 20\,°C$: temperature of the vacuum chamber.

Assuming the detector system to have a surface of $520\,\text{cm}^2$ and be cooled down to a
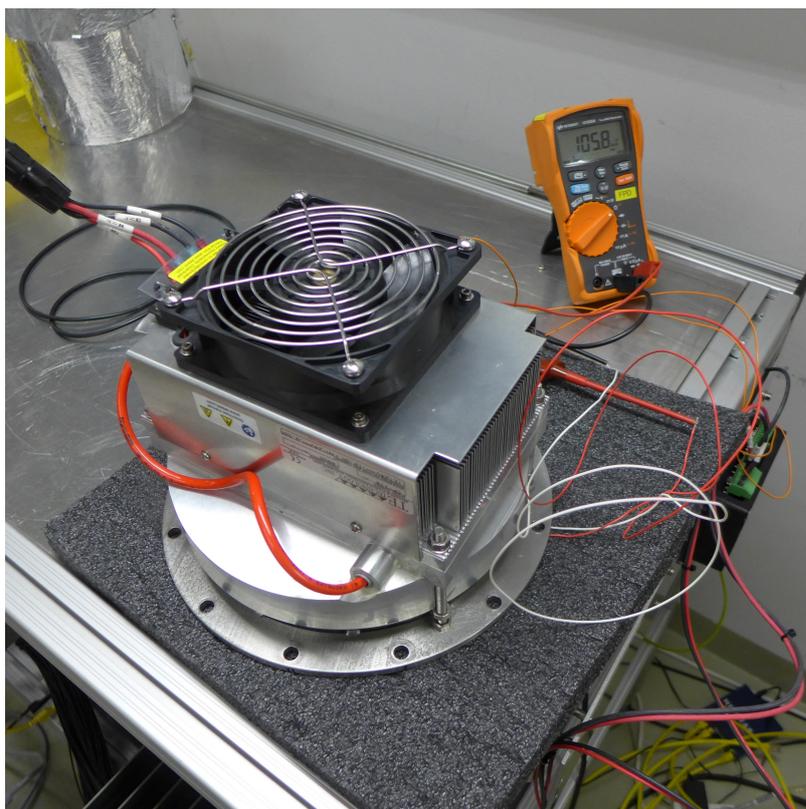
Figure 3.13: **Heat conduction test setup** with detector spare flange, Iron Bird vacuum
flange, Peltier cooler and temperature readout.

temperature of $-15\,°\text{C}$ and the vacuum chamber to be at ambient air tempetature of $20\,°\text{C}$,
the radiative heat flow of $6.6\,\text{W}$ adds up to the heat load of the preamplification cards.
All the preceding measurements were run without any thermal load. Since the source can
illuminate the wafer only quadrant by quadrant, except in the center window, the thermal
load dissipated by the electronics can be reduced by powering only one quadrant. So the
head dissipation reduces to approximately $4.32\,\text{W}$, as deduced in Section 3.3.5. One of this
cooling cycles, recorded with the Pt-1000 mounted on the carousel, is shown in Figure
3.14. At long-term measurements over 145 hours with one powered quadrant the carousel
temperature was $20.9\,°\text{C}$, while the temperature on the preamplification card was $36.9\,°\text{C}$.
The maximum rating for the temperature of the vacuum electronics is $50\,°\text{C}$. By powering
the system with one quadrant the maximum temperature is not exceeded and the Iron
Bird test setup can be operated at a stable temperature. In order to investigate temperature
dependencies and all quadrants powered, the cooling system has to be improved.

3.3.6 Detector Calibration

In order to calibrate the Detector system of the Iron Bird test setup a ^{241}Am γ-source is
used. Since the cooling system is attached to the copper cooling plate five windows have
been milled into the copper plate to insert the γ-source into the system. The five windows
are arranged as shown in Figure 3.15, one window for each quadrant and one for the
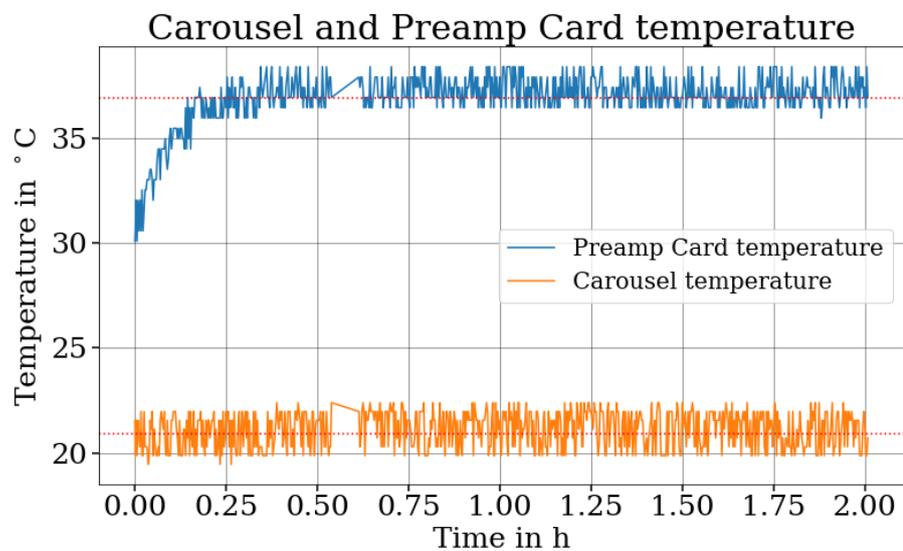
Figure 3.14: **Temperature measurement** of Carousel and Preamplification card with one powered quadrant
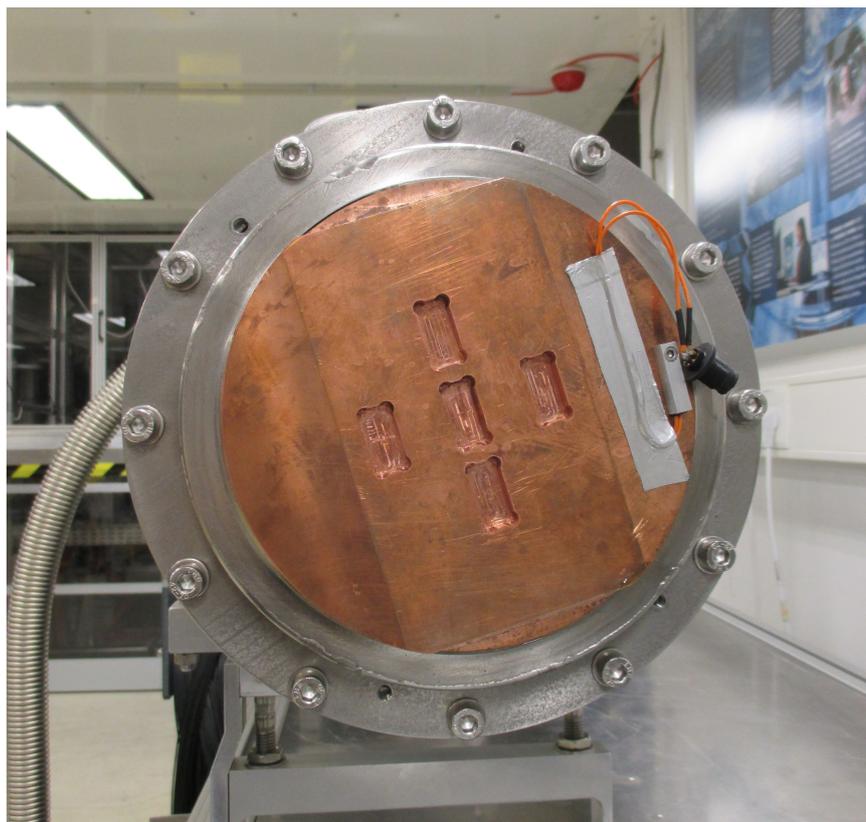
Figure 3.15: **Copper cooling plate** embedded in Iron Bird vacuum flange, with five insertion windows for ^{241}Am γ-source and thermistor of the Peltier cooler.
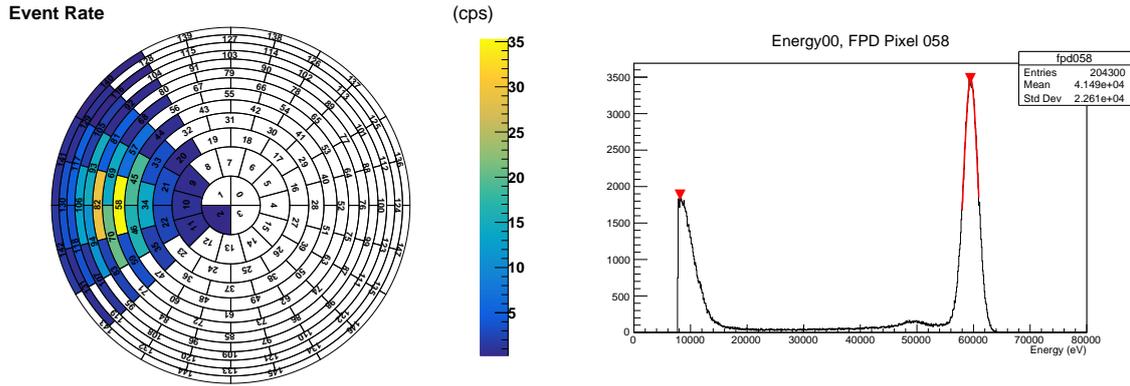
Figure 3.16: **left: Per-pixel rate** with the ^{241}Am-source in the right window, illuminating the left detector quadrant.
right: Energy spectrum of Pixel 58, which is the most illuminated pixel of the right detector quadrant.

bullseye pixels to illuminate every pixel sufficiently. The γ-source is inserted together with a plastic spacer and fixed between the peltier cooler and the cooling plate into the window. As shown in Figure 3.16 (left) one detector quadrant is illuminated. In this case the source was in the right window, illuminating the left quadrant of the detector. For calibrating the detector system the γ-peak of the ^{241}Am-spectrum at 59.54 keV is used. On the right side of Figure 3.16 the already calibrated energy spectrum of the most illuminated Pixel #58 is shown. At the KATRIN FPD system the calibration is accomplished by using the 59.54 keV and additionally the 26.34 keV peak, both shown in Figure 2.6. Due to the copper layer between the source and the detector, which the γs have to penetrate, the lower peak is suppressed in the Iron Bird setup. This effect occurs because the attenuation of radiation penetrating matter is energy-dependent. The intention I of attenuated radiation is given by the Beer-Lambert law:

$$I = I_0 e^{-(\frac{\mu}{\rho}\rho)x} \tag{3.3}$$

where I_0 is the incident intention, μ/ρ the mass attenuation coefficient, ρ the density and x the thickness of penetrated matter.

This yields to a ratio of suppression with an assumed copper layer of $x = 0.3$ mm, the attenuation coefficients $\mu/\rho = 10.1$ cm^2 g^{-1} (30 keV), $\mu/\rho = 1.6$ cm^2 g^{-1} (60 keV) and a density of $\rho = 8.96$ g cm^{-3}:

$$\frac{I_{30\,\text{keV}}}{I_{60\,\text{keV}}} = 10\,\% \tag{3.4}$$

Due to the suppressed 26.34 keV peak the calibration of the detector in the Iron Bird test setup is accomplished by using the peak at 59.54 keV.
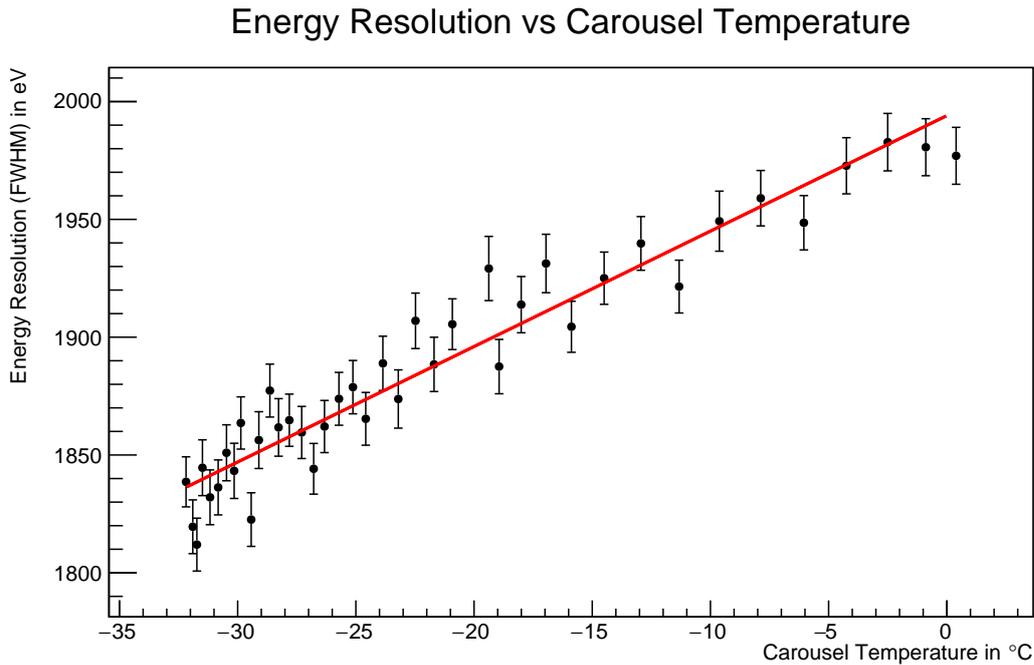
Figure 3.17: **Energy resolution of wafer #96725 as function of the temperature.** A linear dependency of the temperature is seen. The linear fit shown an improvement of energy resolution of $(4.90 \pm 0.20)\,\mathrm{eV\,K^{-1}}$.

3.4 Performance of the KATRIN silicon wafers

In 2019 a batch of two new wafers arrived at the KATRIN experiment. Due to the bad pixels of the wafer mounted in the system in August 2018 a change is considered. To characterize this new batch of wafers the wafer test setup and the Iron Bird test setup were used. The characterization of the wafer mounted in the KATRIN FPD system as well as the two new wafers is the topic of this Section.

3.4.1 Energy resolution of the KATRIN silicon wafers

An important parameter for the characterization of a detector is its energy resolution. This determines the minimal distance between two peaks, which a detector is able to distinguish. To measure the energy resolution of the detector the peak width of the ^{241}Am peak at 59.54 keV is determined. The measured variable is the full width half maximum (FWHM). For this the width of the peak is taken at the half altitude of the maximum peak.

At first the performance of the wafer mounted in the KATRIN Focal Plane Detector system is investigated. After mounting the wafer the cool-down started. During this process the energy resolution in dependency of the temperature was investigated. In Figure 3.17 this dependancy is shown. The linear fit of the data points result in an improvement of energy resolution of $(4.90 \pm 0.20)\,\mathrm{eV\,K^{-1}}$. Additionally in Figure 3.18 (left) the energy resolution of wafer #96725 at the operating temperature of $-25\,^{\circ}$C is shown for each pixel in the
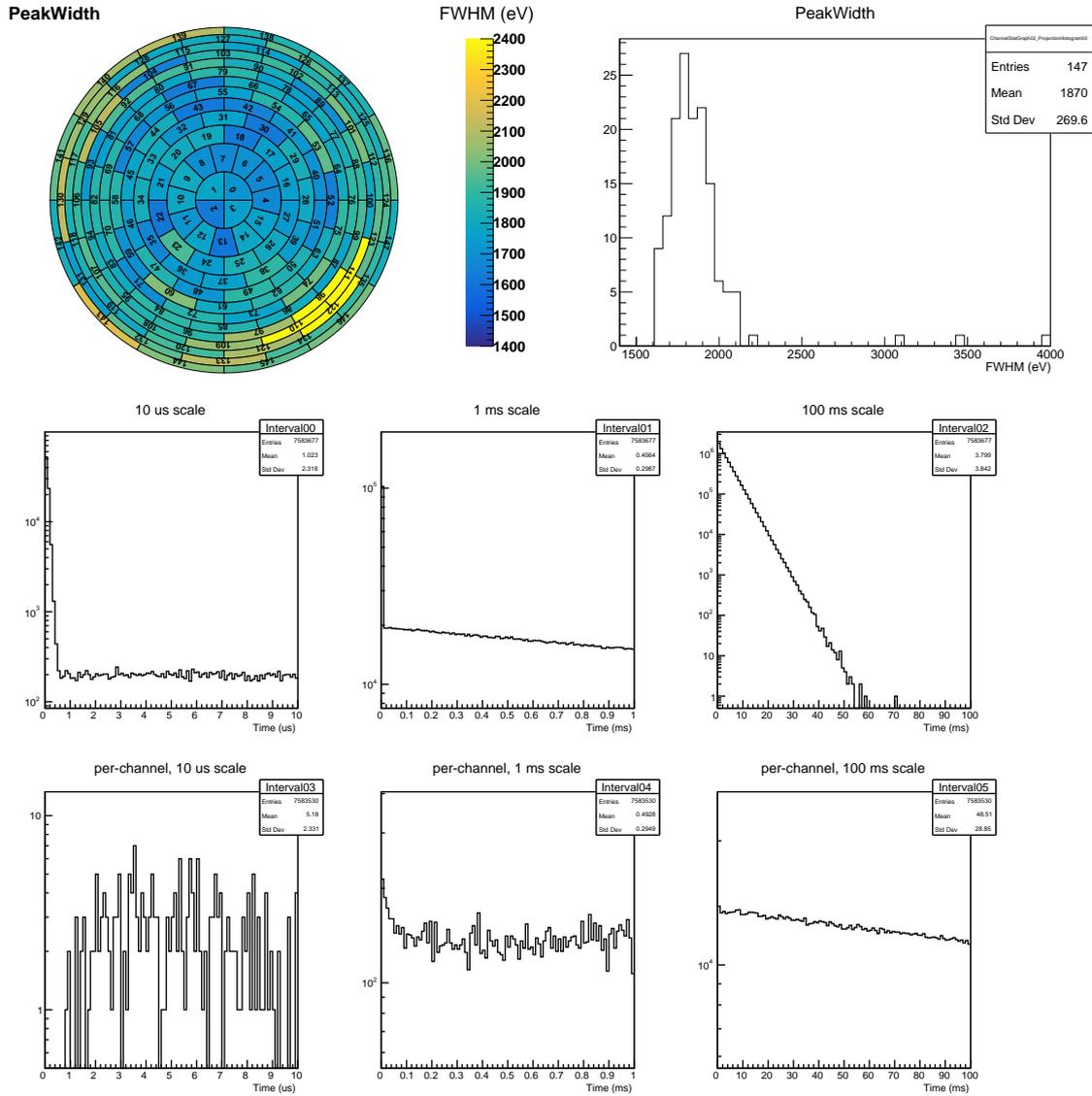
Figure 3.18: **left: Energy Resolution of wafer #96725**, taken with the KATRIN FPD system at a carousel temperature of −20 °C, shown in the dart-board-like segmentation, 12 concentric rings with 12 pixels each and 4 bulls-eye pixels. Pixel 98, 110, 111 122 show an increased energy resolution. Additionally a degraded energy resolution in the outer rings is observable.

right: distribution of energy resolution of wafer #96725 with a mean energy resolution of (1870 ± 260) eV. On the right side of the histogram the damaged pixels 98, 111 and 122 are shown. Pixel 110 was excluded from the analysis due to high noise.

bottom: Distribution of time intervals between events for all events and per-channel events on different time scales: 10 µs, 1 ms and 100 ms. The linear area with $\Delta T > 1$ µs lead from the γ-source. There is no indiation for other sources of noise like clusters and peaks in the time distribution.

dart-board like FPD schematic. Some pixels (98, 110, 111 and 122) show an increased energy resolution. All pixels are located in the same area, so it is probable due to a damaged region on the wafer. The mean energy resolution of wafer #96725 is (1870 ± 260) eV. In Figure 3.18 (right) the distribution of the energy resolution of all pixels is shown. On the right side of the histogram three of the four damaged pixels (98, 111, 122) are shown. Pixel 110 was taken out of the analysis, because the pixel showed very high noise. Additionally an improvement of the energy resolution toward the inner rings is observable.

In order to investigate the performance of the new wafers, they have been mounted in the Iron Bird test setup. At first the wafer with serial number #143109 was mounted. In Figure 3.19 the energy resolution of the new wafer at a mean carousel temperature of 20.89 °C is shown. On the left side the schematic of the wafer in the FPD scheme is shown, while on the right side the distribution of the energy resolutions of wafer #143109 is plotted. Pixel 116, 119, 131, 140 and 143 are excluded from analysis due to insufficient statistics. Pixel 87 shows a high energy resolution. As with wafer #96725 a degradation of the energy resolution towards the outer rings can be seen. The mean energy resolution is given by (3160 ± 230) eV.

When the measurements with wafer #143109 were finished the second wafer #143110 was mounted into the Iron Bird. In Figure 3.20 both the energy resolution of this wafer in the FPD scheme and the distribution of energy resolutions is shown. The mean carousel temperature was 13.00 °C. Pixel 141 shows a high energy resolution. Again a degradation of the energy resolution towards the outer rings is observable. The mean energy resolution of wafer #143110 is given by (2890 ± 150) eV.

Assuming a linear degradation of energy resolution with rising temperature of 4.90 eV K^{-1} the energy resolution of wafer #96728 results in 2087 eV at $T = 20$ °C. Compared to this both wafers of the new batch have a worse energy resolution with (3160 ± 230) eV (#143109 at $T = 13.00$ °C and (2890 ± 150) eV at $T = 20$ °C.

3.4.2 Inter-arrivel time distribution

In order to examine the system for noise and background the inter-arrival time distribution is plotted. The time difference between two consecutive events is measured for all pixels and seperately for each individual pixel. For a Poisson distributed event rate, like the γs emitted by the ^{241}Am source, the probability function for the time difference t between two consecutive events is given by [57]:

$$f(t) = \lambda e^{-\lambda t} \tag{3.5}$$

On a logarithmic scale on the y-axis a Poisson distributed source causes a linear distribution in inter-arrival times.

In Figure 3.18 (bottom) the inter-arrival time distributions for the FPD wafer (#96725) are shown. On the upper figure the distribution of the inter-arrival time of all events is shown,
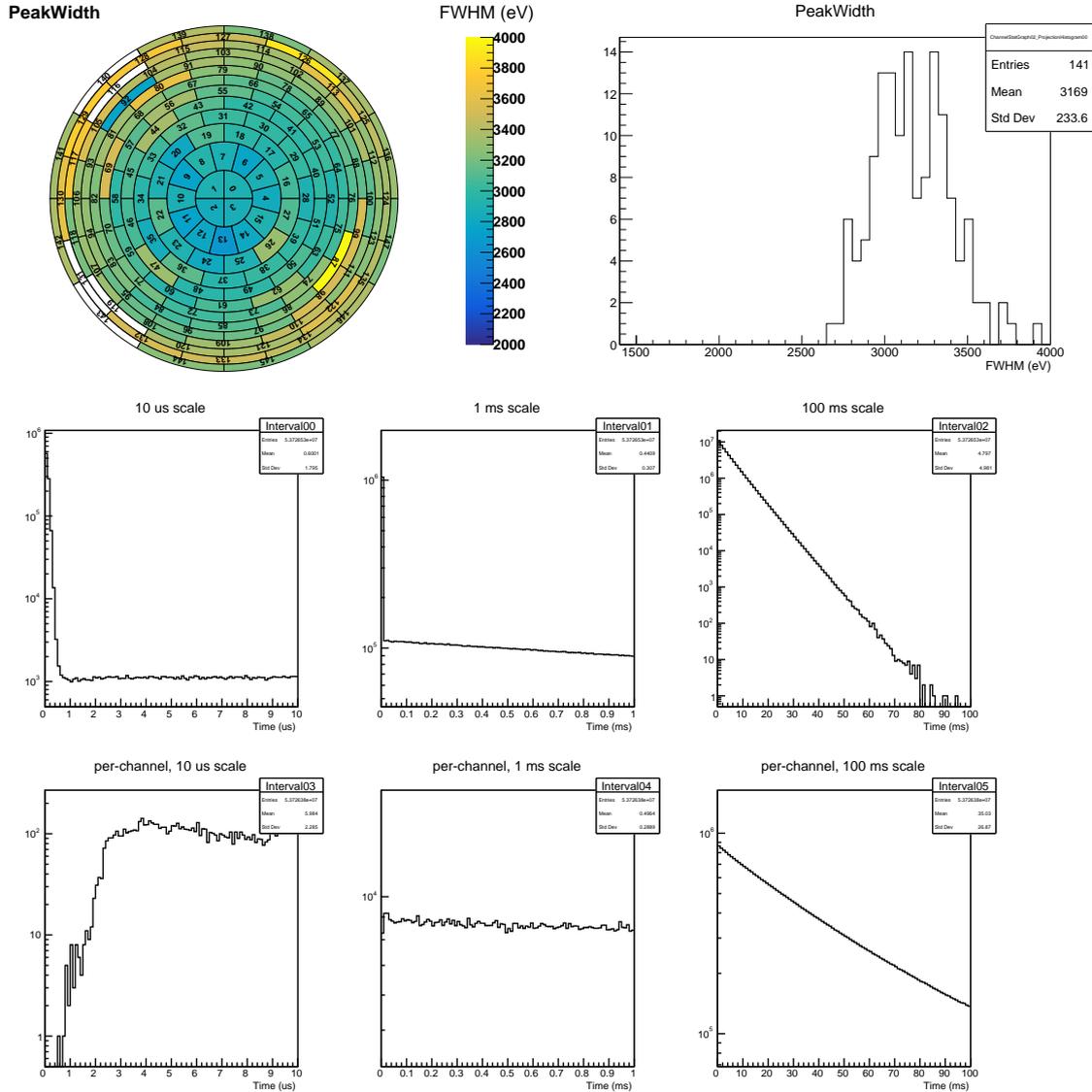
Figure 3.19: **left: Energy Resolution of wafer #143109**, taken with the Iron Bird test setup at a carousel temperature of 13.00 °C, shown in the dart-board-like schematic. Pixel 116, 119, 131, 140 and 143 are excluded from analysis due to insufficient statistics. Pixel 87 shows a high energy resolution. Additionally a degradation of the energy resolution towards the outer rings is observable.
right: distribution of energy resolution of wafer #143109 with a mean energy resolution of (3160 ± 230) eV.
bottom: Distribution of time intervals between events for all events and per-channel events on different time scales: 10 µs, 1 ms and 100 ms. The linear area with $\Delta t > 1$ µs lead from the γ-source. There is no indiation for other sources of noise like clusters and peaks in the time distribution.

Figure 3.20: **left: Energy Resolution of wafer #143110**, taken with the Iron Bird test setup at a carousel temperature of 20 °C, shown in the dart-board-like schematic. A degradation of the energy resolution towards the outer rings is observable.

right: distribution of energy resolution of wafer #143110 with a mean energy resolution of (2890 ± 150) eV.

bottom: Distribution of time intervals between events for all events and per-channel events on different time scales: 10 µs, 1 ms and 100 ms. The linear area with $\Delta T > 1\,\mu s$ lead from the γ-source. There is no indiation for other sources of noise like clusters and peaks in the time distribution.

while in the lower figure only consecutive events of the same channel are considered. The linear distribution for $\Delta T > 1\,\mu s$ for all events is caused by the γ-source. In the area of $\Delta T < 1\,\mu s$ the distribution shows a second slope, which is caused by other effects like charge sharing or between two neighboring pixels or cosmic muons. In the per-channel distributions for the time scale of 1 ms a raise at lower times for $T < 0.1\,ms$ can be observed. This is a possible indicator for events induced by cosmical muons. The drop in the per-channel distribution to lower time differences shown in the per-channel distribution at a timescale of $10\,\mu s$ is caused by the shaping time of $1.6\,\mu s$. For non-poissonial sources of events like electronical noise one would expect clusters in the inter-arrival time distribution, which are not observable. [31]

The inter-arrivel time distribution of wafer #143109 is shown in Figure 3.19. In the $10\,\mu s$ timescale of all events two slopes are observable. The slope with inter-arrival times higher than $1\,\mu s$ are caused by the used ^{241}Am source. The slope at lower times is caused by other effects like charge sharing or cosmic muons. At the time scale of $100\,\mu s$ both all events and per-channel events show a approximately linear regime without clusters, which would indicate noise. At lower times of $T < 10\,\mu s$ the per-channel events with inter-arrival times of $\Delta T < 1.6\,\mu s$ drop due to the shaping length.

In Figure 3.20 the inter-arrival time distribution of wafer #143110 is shown. Both the two slopes of the source and other effects like charge sharing or cosmic muons is observable. Additionally the drop at lower time differences is shown. No indication for noise can be seen in the inter-arrival time distributions.

3.4.3 Analysis of noise spectrum

An additional possibility of investigating noise is the noise spectrum. Therefor the waveform signals are recorded in energy and trace mode, as shown in Table 3.1 and then converted with a Fast Fourier transform (FFT) into the freqency domain. In this spectrum it is possible to examine resonances and frequency-dependent influences, that effect the detector signal. This noise spectra for wafer #96725, #134109 and #134110 are shown in Figure 3.21. Each spectra is a composition of several influences. A good model for the noise of the detector system is a composition of white noise, red noise and pink noise. The thermal agitation of the charge carriers inside an electrical conductor generate Johnson noise. Every conductor in the detector system causes this kind of noise. White noise is generated mainly by the series resistance of the detector, which causes voltage noise. This noise is independent from frequency and leads to a plateau in the noise spectrum. Red noise is generated by leakage current and parallel resistance, which lead to current noise. Red noise has a frequency dependence of $\frac{1}{f^2}$. Additionally pink noise is generated by semiconductors and have a freqency dependence of $\frac{1}{f}$. Red and pink noise generate a steep slope towards lower frequencies in the noise spectrum. Since the detector possesses an intrinsic capacitance of $8.2\,pF$ per pixel it behaves like a low pass filter, which yields to a cutoff at high frequencies. In Figure 3.21 the noise spectra of wafer #96725 (top), #143109 (middle) and #143110 (bottom) is shown. Wafer #96725 shows a plateau in the
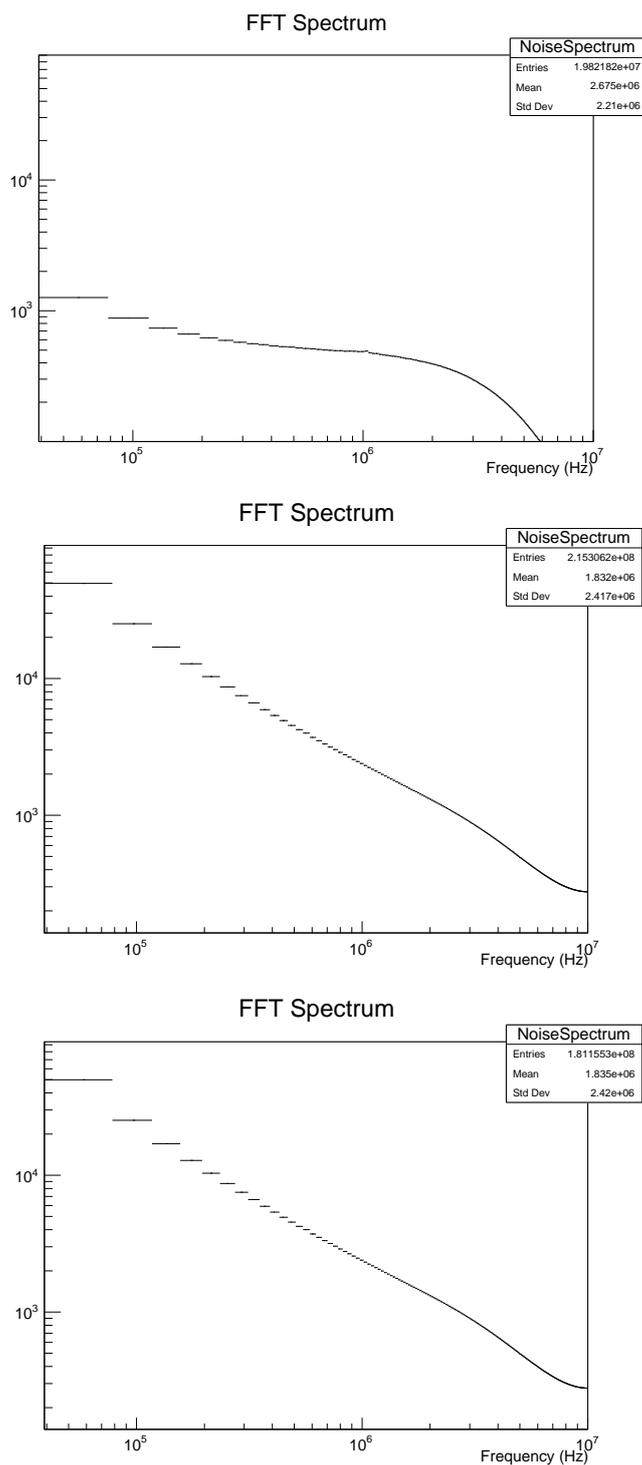
Figure 3.21: **Noise spectra of wafer #96725 (top)** with a plateau, generated by white noise. No peak structures of microphonics and electromagnetic interference observable.

Noise spectrum of wafer #143109 (middle) with red and pink noise dominated spectrum and no peak structures.

Noise spectrum of wafer #143110 (bottom) with red and pink noise dominated spectrum and no peak structures.

noise spectrum, which is generated by white noise. The noise spectra of the new wafers are dominated by red and pink noise, which can be attributed to the higher temperature, since the leakage current is exponentially and the Johnson noise is linearly temperature-dependent. A peak structure which would indicate microphonics and electromagnetic interference is not observable and can be excluded.[58]

After determination of the energy resolution, analysis of the inter-arrival times and noise investigation with the Iron Bird test setup, the energy resolutions of the new batch of wafers with 3169 eV for wafer #143109 and 2897 eV for wafer #143110 are higher than the extrapolated energy resolution of wafer #96725 with 2087 eV. This leads to the conclusion, that the KATRIN wafers of the new batch are no suitable candidates for the replacement of the KATRIN FPD wafer.

4 Conclusion

The Focal Plane Detector system has to detect electrons in a wide energy range both with a high efficiency and good energy resolution. This is provided by a silicon PIN diode, mounted in the detector system. During SDS3c in 2017 a wafer was damaged and had to be replaced. The fresh mounted wafer turned out to have an area of bad energy resolution. In 2012 a wafer was installed with two shorted pixels. In order to characterize potential replacement wafers, two test stands have been established at KIT. With a Wafer test board a wafer can be examined for short-circuits between adjacent pixels. In order to investigate the energy resolution of a wafer a test setup called the Iron Bird has been established. With its readout and data-acquisition system equivalent to the KATRIN FPD it provides a suitable tool for wafer characterization.

In 2019 a batch of two wafers arrived at KIT, which had to be investigated for their suitability to replace the currently installed wafer in the KATRIN FPD, due to a area of bad energy resolution. Both wafers have been tested successfully with the Wafer test board for short-circuits. Due to cooling issues with the Iron Bird test setup a few investigation regarding the cooling of the detector system inside the vacuum were performed. The thermal contact between the copper cooling plate of the used Peltier cooler and a spare detector flange was investigated in ambient air, with promising results. Another measurement with Pt-100 temperature sensors installed in the Iron Bird vacuum chamber, led to the result of a poor thermal contact, which is still an issue. However, by powering the system with one quadrant a stable operation in thermal equilibrium is possible.

Using this configuration the two wafers with serial numbers #143109 and #143110 were characterized with the Iron Bird test setup with the following results: The mean energy resolution of wafer #143109 is given by: (3160 ± 230) eV at a temperature of 20.89 °C with Pixel 87 showing a high energy resolution. Whereas the mean energy resolution of wafer #143110 results in (2890 ± 150) eV at a temperature of 13.00 °C. On both wafers a degradation of energy resolution towards the outer rings is observable. The inter-arrival times of the events showed no indication for noise induced events. Additionally the noise spectra of both wafers showed no indication for microphonics or electromagnetic interference. The currently in the KATRIN FPD installed wafer #96725 showed the same results, only red and pink noise is reduced compared to the new wafers, due to a lower temperature of −20 °C. Extrapolating the energy resolution of this wafer from 1870 eV at −20 °C to 2087 eV at 20 °C leads to the conclusion, that both new wafers have a worse energy resolution excluding them as candidates for the considered wafer exchange of the KATRIN FPD wafer.

List of Figures

List of Tables

Bibliography

[1] W. Pauli. "Offener Brief an die Gruppe der Radioaktiven bei der Gauvereins-Tagung zu Tubingen". In: (1930). URL: http://www.symmetrymagazine.org/sites/default/files/legacy/pdfs/200703/logbookletter.pdf.

[2] C. Cowan and F. Reines. "Detection of the Free Neutrino: a Confirmation". In: *Science* 124.3212 (1956). DOI: 10.1126/science.124.3212.103.

[3] F. A. Scott. "Energy Spectrum of the Beta Rays of Radium E". In: *Phys. Rev.* 48.5 (1935). DOI: 10.1103/PhysRev.48.391.

[4] E. Fermi. "Versuch einer Theorie der Beta-Strahlen. I". In: *Zeitschrift fur Physik* 88.3–4 (1934). DOI: 10.1007/BF01351864.

[5] F. Reines and C. L. Cowan. "Detection of the Free Neutrino". In: *Physical Review* 92 (3 1953), pp. 830–831. DOI: 10.1103/PhysRev.92.830.

[6] G. Danby et al. "Observation of High-Energy Neutrino Reactions and the Existence of Two Kinds of Neutrinos". In: *Phys. Rev. Lett.* 9.1 (1962). DOI: 10.1103/PhysRevLett.9.36.

[7] DONUT Collaboration. "Observation of Tau Neutrino Interactions". In: *Phys. Lett. B* 504.3 (2001). DOI: 10.1016/S0370-2693(01)00307-0.

[8] J. N. Bahcall et al. "New Solar Opacities, Abundances, Helioseismology, and Neutrino Fluxes". In: *The Astrophysical Journal Letters* 621.1 (2005). DOI: 10.1086/428929.

[9] ATLAS Collaboration. "Observation of a new particle in the search for the Standard Model Higgs boson with the ATLAS detector at the LHC". In: *Physics Letters B* 716.1 (2012). DOI: 10.1016/j.physletb.2012.08.020.

[10] CMS Collaboration. "Observation of a new boson at a mass of 125 GeV with the CMS experiment at the LHC". In: *Physics Letters B* 716.1 (2012). DOI: 10.1016/j.physletb.2012.08.021.

[11] C. S. Wu et al. "Experimental Test of Parity Conservation in Beta Decay". In: *Phys. Rev.* 105.4 (1957). DOI: 10.1103/PhysRev.105.1413.

[12] M. Goldhaber, L. Grodzins, and A. W. Sunyar. "Helicity of neutrinos". In: *Phys. Rev.* 109 (1958), pp. 1015–1017.

[13] D. DeCamp and others (ALEPH Collaboration). "Determination of the number of light neutrino species". In: *Phys. Lett. B* 231.4 (1989), pp. 519–529. DOI: 10.1016/0370-2693(89)90704-1.

[14] J. C. Evans R. Davis Jr. and B. T. Cleveland. "The solar neutrino problem". In: *AIP Conf. Proc.* 52.17 (1979). DOI: 10.1063/1.31802.

[15] J. N. Bahcall. "Solar Neutrino Cross Sections and Nuclear Beta Decay". In: *Phys. Rev.* 131.1 (1964). DOI: 10.1103/PhysRev.135.B137.

[16] GALLEX Collaboration. "GALLEX solar neutrino observations: results for GALLEX IV". In: *Physics Letters B* 447.1-2 (1999), pp. 127–133. DOI: 10.1016/S0370-2693(98)01579-2.

[17] J. N. Abdurashitov, E. P. Veretenkin, V. M. Vermul, et al. "Solar neutrino flux measurements by the Soviet-American gallium experiment (SAGE) for half the 22-year solar cycle". In: *Journal of Experimental and Theoretical Physics* 95.2 (2002), pp. 181–193. DOI: 10.1134/1.1506424.

[18] GNO Collaboration. "Complete results for five years of GNO solar neutrino observations". In: *Physics Letters B* 616.3-4 (2005), pp. 174–190. DOI: 10.1016/j.physletb.2005.04.068.

[19] K. S. Hirata et al. "Experimental study of the atmospheric neutrino flux". In: *Phys. Lett. B* 205.2-3 (1922), pp. 416–420. DOI: 10.1016/0370-2693(88)91690-5.

[20] B. Aharmim et al. (SNO Collaboration). "Combined analysis of all three phases of solar neutrino data from the Sudbury Neutrino Observatory". In: *Phys. Rev. C* 88 (2013), p. 025501. DOI: 10.1103/PhysRevC.88.025501.

[21] L. Wolfenstein. "Neutrino oscillations in matter". In: *Physical Review D* 17.9 (1978). DOI: 10.1103/PhysRevD.17.2369.

[22] S. F. King and C. Luhn. "Neutrino mass and mixing with discrete symmetry". In: *Reports on Progress in Physics* 76.5 (2013). DOI: 10.1088/0034-4885/76/5/056201.

[23] S. Fukuda and others (Super-Kamiokande Collaboration). "Determination of solar neutrino oscillation parameters using 1496 days of Super-Kamiokande-I data". In: *Phys. Lett. B* 539 (2002), pp. 179–187. DOI: 10.1016/S0370-2693(02)02090-7.

[24] F. P. An and others (Daya Bay Collaboration). "Observation of Electron-Antineutrino Disappearance at Daya Bay". In: *Phys. Rev. Lett.* 108 (2012), p. 171803. DOI: 10.1103/PhysRevLett.108.171803.

[25] Y. Abe and others (Double Chooz Collaboration). "Reactor $\bar{\nu}_e$ disappearance in the Double Chooz experiment". In: *Phys. Rev. D* 86 (2012), p. 052008. DOI: 10.1103/PhysRevD.86.052008.

[26] Ivan Esteban et al. "Global analysis of three-flavour neutrino oscillations". In: *JHEP* 01 (2019). DOI: 10.1007/JHEP01(2019)106.

[27] M. Schlösser. "Accurate calibration of the raman system for the karlsruhe tritium neutrino experiment". In: *Ph.D. dissertation, Karlsruher Institut für Technologie (KIT)* (2013).

[28] S. R. Elliott and P. Vogel. "Double beta decay". In: *Annual Review of Nuclear and Particle Science* 52.1 (2002).

[29] Planck Collaboration. "Planck 2013 Results. XVI. Cosmological Parameters". In: *Astronomy and Astrophys.* 571 (2014).

[30] K. Ackermann et al. (GERDA Collaboration). "The Gerda experiment for the search of $0\nu\beta\beta$ decay in ^{76}Ge". In: *The European Physical Journal C* 73.1 (2013). DOI: `10.1140/epjc/s10052-013-2330-0`.

[31] Marc Korzeczek. "Detection Efficiency for KATRIN". In: (2017). URL: `http://neutrino.ikp.kit.edu/katrin/images/4/43/MK-DetEfficiency.pdf`.

[32] The Majorana Collab. "The Majorana Ge-76 Double-Beta Decay Project". In: *arXiv:051301* (2002).

[33] C. Arnaboldi et al. "CUORE: a cryogenic underground observatory for rare events". In: *Nuclear Instruments and Methods in Physics Research Section A: Accelerators, Spectrometers, Detectors and Associated Equipment* 518.3 (2004). DOI: `10.1016/j.nima.2003.07.067`.

[34] M. Tanabash and others (Particle Data Group). "Double beta decay". In: *Phys. Rev. D* 98.1 (2018).

[35] C. Kraus et al. "Final results from phase II of the Mainz neutrino mass search in tritium β decay". In: *The European Physical Journal C* 40.4 (2005), pp. 447–468. DOI: `10.1140/epjc/s2005-02139-7`.

[36] V. N. Aseev et al. "Upper limit on the electron antineutrino mass from the Troitsk experiment". In: *Physical Review D* 84 (11 2011), p. 112003. DOI: `10.1103/PhysRevD.84.112003`.

[37] G. Beamson, H. Q. Porter, and D. W. Turner. "The collimating and magnifying properties of a superconducting field photoelectron spectrometer". In: *Journal of Physics E: Scientific Instruments* 14.2 (1981), p. 256. DOI: `10.1088/0022-3735/14/2/526`.

[38] N. Wandkowski. "Study of background and transmission properties of the KATRIN spectrometers". In: *Dissertation, Karlsruhe Institut für Technologie* (2013).

[39] J. Angrik et al. "KATRIN Design Report 2004". In: *FZKA Scientific Report 7090* (2005).

[40] S. Rupp. "Development of a highly sensitive hollow waveguide based Raman system for the compositional analysis of the KATRIN tritium source gas". In: *PhD thesis, Karlsruhe Institut für Technologie* (2016).

[41] F. Harms. "Assembly and First Results of the KATRIN Focal-Plane Detector System at KIT". In: *PhD thesis, Karlsruhe Institut für Technologie* (2012).

[42] M. Babutzka et al. "Monitoring of the operating parameters of the KATRIN Windowless Gaseous Tritium Source". In: *New Journal of Physics* 14.10 (2012), p. 103046. DOI: `10.1088/1367-2630/14/10/103046`.

[43] S. Grohmann et al. "The thermal behaviour of the tritium source in KATRIN". In: *Cryogenics* 55-56.10 (2013), pp. 5–11.

[44] S. Grohmann et al. "Precise temperature measurement at 30 k in the KATRIN source cryostat". In: *Cryogenics* 51.8 (2011), pp. 438–445.

[45] F. Friedel et al. "Time dependent simulation of the flow reduction of D_2 and T_2 in the KATRIN experiment". In: *Vacuum* 159.10 (2019), pp. 161–172. DOI: 10.1016/j.vacuum.2018.10.002.

[46] X. Luo et al. "Monte Carlo simulation of gas flow through the KATRIN DPS2-F differential pumping system". In: *Vacuum* 80.8 (2006), pp. 864–869. DOI: 10.1016/j.vacuum.2005.11.044.

[47] M. Ubieto-Diaz et al. "A broad-band FT-ICR Penning trap system for KATRIN". In: *International Journal of Mass Spectrometry* 288.1-3 (2009), pp. 1–5. DOI: 10.1016/j.ijms.2009.07.003.

[48] M. Ubieto-Diaz. "Off-line commissioning of a non-destructive FT-ICR detection system for monitoring the ion concentration in the KATRIN beamline". In: *doctoral thesis, Ruprecht-Karls-Universität, Heidelberg, Germany* (2011).

[49] Alexander Windberger. "Berechnungen und Simulationen zum Verhalten von Ionen in der differenziellen Pumpstrecke des KATRIN-Experiments". In: *Diploma Thesis, Karlsruher Institut für Technologie (KIT)* (2011). URL: http://www.katrin.kit.edu/publikationen/dth-windberger.pdf.

[50] Stefan Reimer. "Ein elektrostatisches Dipolsystem zur Eliminierung von Ionen in der DPS2-F des KATRIN Experimentes". In: *Diploma Thesis, Karlsruher Institut für Technologie (KIT)* (2009). URL: http://www.katrin.kit.edu/publikationen/dth-reimer.pdf.

[51] W. Gil et al. "The Cryogenic Pumping Section of the KATRIN Experiment". In: *IEEE Transactions on Applied Superconductivity* 20.3 (2010), pp. 316–319. DOI: 10.1109/TASC.2009.2038581.

[52] J. F. Amsbaugh et al. "Focal-plane detector system for the KATRIN experiment". In: *NIM A* (2014). DOI: arXiv:1404.2925[physics.ins-det].

[53] E. L. Martin. "FPD Wafer Test Board". In: *internal KATRIN document* (2014). URL: http://fuzzy.fzk.de/bscw/bscw.cgi/d875187/FPDWaferTester.pdf.

[54] B. L. Wall et al. "Dead layer on silicon p-i-n diode charged-particle detectors". In: *NIM A* (2014). DOI: arXiv:1310.1178[physics.ins-det].

[55] J. Schwarz. "Implementation and first measurements with the spectrometer". In: *dissertation, Karlsruhe Institut für Technologie* (2014).

[56] Inc. TE Technology. "CP-110 Peltier-Thermoelectric Cold-Plate Cooler". In: (2018). URL: https://tetech.com/files/cold_plate/CP-110.pdf.

[57] R. Waldi. "Statistische Datenanalyse: Grundlagen und Methoden fur Physiker". In: *Springer Spektrum* (2015).

[58] S. Enomoto. "FPD Noise Analysis". In: *presentation* (2013).